nature cardiovascular research

Article

https://doi.org/10.1038/s44161-025-00717-y

Spatial multiomics of acute myocardial infarction reveals immune cell infiltration through the endocardium

Received: 24 April 2024

Accepted: 20 August 2025

Published online: 03 October 2025

Check for updates

Florian Wünnemann[1,2,11], Florian Sicklinger[3,4,11], Kresimir Bestak[1], Jose Nimo[5,6], Tobias Thiemann[3,4], Junedh M. Amrute[7], Mathias Nordbeck[1], Niklas Hartmann[3,4], Miguel A. Ibarra-Arellano[1], Jovan Tanevski[1,8], Margot Chazotte[1], Clara Heine[3,4], Norbert Frey[3,4], Kory J. Lavine[7], Fabian Coscia[5], Julio Saez-Rodriguez[1,9], Florian Leuschner[3,4,11] ✉ & Denis Schapiro[1,8,10,11] ✉

Myocardial infarction (MI) continues to be a leading cause of death worldwide. Even though it is well established that the complex interplay between different cell types determines the overall healing response after MI, the precise changes in the tissue architecture are still poorly understood. In this study, we generated an integrative cellular map of the acute phase after murine MI using a combination of imaging-based transcriptomics (Molecular Cartography) and antibody-based highly multiplexed imaging (Sequential Immunofluorescence). This enabled us to evaluate cell type compositions and changes at subcellular resolution over time. We observed the recruitment of leukocytes to the infarcted heart through the endocardium and performed unbiased spatial proteomic analysis using Deep Visual Proteomics (DVP) to investigate the underlying mechanisms. DVP identified von Willebrand factor (vWF) as an upregulated mediator of inflammation 24 hours after MI, and functional blocking of vWF reduced the infiltration of C-C chemokine receptor 2 (Ccr2)-positive monocytes and worsened cardiac function after MI.

Myocardial infarction (MI) is an acute disease characterized by large shifts in cellular composition and tissue architecture due to cell death of cardiac muscle tissue caused by local hypoxia[1]. MI remains one of the leading causes of death worldwide, despite considerable improvements in the prevention and treatment of the disease[2,3]. Although advancements in restoring blood flow to the heart muscle (termed reperfusion) and pharmacological treatment strategies have largely reduced short-term deaths, long-term mortality after MI continues to be high[4–6]. One of the reasons why mortality remains high is that we do not understand how molecular cues and tissue microenvironment alterations during acute disease affect healing and remodeling in the long run. During an acute infarct, necrotic cells in the heart release stress signals, including pro-inflammatory cytokines and chemokines, leading to the invasion of the infarct zone by immune cells—specifically neutrophils, monocytes/macrophages (Mo/Mϕ) and later T cells, B cells and natural killer cells[1,7–10]. Modulation of the types and amount of immune cells infiltrating the infarct have been postulated as potential treatment targets to improve healing and outcome after MI[11,12]. A better understanding of the immune cell infiltration routes and pathways, detailed tissue microenvironment and cellular interactions in the heart during the early phases of MI thus holds the promise to deliver potential novel treatment strategies.

Extensive research has been performed on the temporal dynamics of immune cell infiltration during the course of MI in humans and

A full list of affiliations appears at the end of the paper. ✉e-mail: florian.leuschner@med.uni-heidelberg.de; denis.schapiro@uni-heidelberg.de

mice[1,8,13,14]. Cell count estimations of the immune infiltrate have been generated using fluorescence-activated cell sorting (FACS) of left ventricular cardiac tissue[14–17]. Single-cell RNA sequencing (scRNA-seq) provided further insight into the diverse subtypes of immune cells that infiltrate the necrotic myocardium and their different pathway activities and physiological roles[18–21]. Two recent studies applied single-nucleus RNA sequencing (snRNA-seq) alongside untargeted spatial transcriptomics to investigate the border infarct zone during MI in mice[22,23]. Combining the spatial readout with transcriptome-wide measurements, both studies identified important transcriptional signatures of the infarct border zone. Another large study generating a spatial multiomic map of human MI also used untargeted transcriptomics to investigate the different cell neighborhoods and tissue architectures during MI progression in humans[24]. Although these studies were able to connect critical molecular patterns and processes during MI to their spatial context, they could not accurately quantify the tissue microenvironment and cellular neighborhoods, due to the limited spatial resolution (approximately 55 µm) of the technology used, which effectively captures a mix of 10–20 cells per measurement. Novel targeted spatial omics technologies with subcellular resolution are transforming our understanding of tissue architecture and the corresponding cell type interactions in health and disease[25,26]. Highly multiplexed approaches to measure tens to thousands of transcripts, antibodies or both combined enable a detailed description of the changing cellular phenotypes and neighborhoods during homeostasis and disease[27–30]. Furthermore, developments in computer vision now enable cell identification using automated cell segmentation and classification algorithms[31–34].

In the present study, we used combinatorial imaging technologies based on RNA detection via fluorescence in situ hybridization (FISH) barcoding (Molecular Cartography) and antibody-based Sequential Immunofluorescence (SeqIF, Lunaphore COMET), respectively, to characterize the changing tissue microenvironment during acute MI in mice. Subsequently, we developed scalable computational pipelines (nf-core/molkart) tailored for cardiac tissues, using state-of-the-art methodology to process these complex, highly multiplexed imaging datasets. Using Molecular Cartography and SeqIF across a time-course of the acutely infarcted heart (control prior to infarct, 4 hours, 24 hours, 2 days and 4 days after MI), in a minimally invasive MI model, we were able to characterize the acute MI microenvironment at single-cell resolution[35]. From this spatiotemporal map of MI, we discovered that myeloid cells (specifically Mo/Mϕ) enter the infarct region not only via the border and epicardial infarct zone but also via the endocardial infarct zone, which was previously unknown. Laser microdissection of endocardial regions 24 hours after infarction followed by ultrasensitive proteomics was performed to investigate this infiltration route, which revealed local signatures of inflammation and coagulation factors and highlighted vWF as an immune mediating agent in endocardial cells[36]. To further investigate the role of vWF, antibody-based functional blocking of vWF during the first day after MI showed a significant reduction of Mo/Mϕ infiltration via the endocardial route and reduced left ventricular function. Therefore, our study highlights, to our knowledge for the first time, a critical role of the endocardium for infiltration of immune cells into the infarct via local upregulation of adhesion factors such as vWF. These results highlight previously unknown routes of immune cell infiltration and provide novel potential targets for pharmacological intervention.

Results

Single-cell resolved spatial transcriptomic analysis of acute MI

To characterize the cellular environment during homeostasis and acute MI in the mouse heart, we used a combinatorial single-molecule FISH (smFISH)-based technology called Molecular Cartography by Resolve Biosciences (Fig. 1a and Extended Data Fig. 1a–c). Molecular Cartography allows for the detection of RNA transcripts for up to 100 candidate genes at single-molecule resolution with high sensitivity in selected regions of interest (ROIs). Based on marker gene expression from existing publicly available scRNA-seq datasets and expert knowledge, we subsequently designed a 100-gene transcript panel specifically for this study, to capture major cell types as well as inflammatory signals during acute MI (Supplementary Table 1)[37–41]. Using this panel, we selected one ROI per heart (2.09 mm^2 to 2.97 mm^2) cross-section to measure endocardial, myocardial and epicardial regions at four different timepoints during acute MI (control prior to infarct, 4 hours, 2 days and 4 days) (Extended Data Fig. 1a–c). Identification and abundance of RNA transcript spots were highly reproducible across technical replicate slides of Molecular Cartography, as highlighted by a strong correlation of pseudobulk transcript counts across sections from the same biological sample (Supplementary Fig. 1a). On average across all timepoints, we detected 980,000 RNA transcript spots per mm^2 of heart tissue with lower transcript density in infarcted tissues due to fewer viable cells within the infarct region (Supplementary Fig. 1b). Principal component analysis (PCA) of pseudobulk transcriptional profiles showed separation of samples by time relative to the induced infarct, confirming strong transcriptional shifts in response to acute infarction (Supplementary Fig. 1c). For each timepoint (control, 4 hours, 2 days and 4 days), we assayed two biological replicates using Molecular Cartography and processed the data with an in-house-developed, open-source computational pipeline that we call nf-core/molkart (Fig. 1b). Despite advances in deep-learning-based methods, segmentation of cardiac cells from microscopy images remains extremely challenging due to their differences in cell size, shape, orientation, multinucleation and RNA content. Comparing four different cell segmentation approaches (DeepCell Mesmer's 'nuclear' and 'whole-cell' models, the Cellpose cytoplasmic model ('cyto') and a custom Cellpose 2 model), we found that Cellpose with a human-in-the-loop trained model performed best on our murine cardiac tissue samples when evaluating against independently annotated ground truth segmentations; it also showed an overall higher percentage of assigned RNA spots to cells (Extended Data Fig. 2)[33,34,42]. Cell typing of cell transcript profiles across all images (69,028 cells in total, average number of cells per sample = 8,629) identified all major cardiac cell types during acute MI (Fig. 1c). We found healthy as well as stressed cardiomyocytes distinguished by their expression of atrial natriuretic peptide (Nppa) and brain natriuretic peptide (Nppb), cells of the vasculature (pericytes, smooth muscle cells and endothelial cells), cardiac fibroblasts as well as infiltrating myeloid and lymphoid cells (Fig. 1d). The hypoxic environment in the left ventricle during acute MI leads to massive cell death and changes in tissue composition and architecture within the left ventricle. In line with these expectations and known cell dynamics from literature, we observed a strong shift in the cell type composition from healthy to infarcted left ventricular tissue during the first 4 days after MI (Extended Data Fig. 3a,b). Healthy left ventricular tissue composed of cardiomyocytes, endothelial cells and fibroblasts showed compositional changes toward an environment of dying and stressed cardiomyocytes ($Nppa^+$) surrounded by extracellular matrix (ECM)-producing cardiac fibroblasts and invading myeloid cells after MI. Because our selected ROI contained large areas of infarct tissue, healthy cardiomyocytes showed the highest decrease in cell number from an average of 57.9% of identified cells in controls to only about 10% at day 4 in the processed regions. In line with increased ECM production and early scar formation, cardiac fibroblasts increased from 6.6% to 30.8% of cells within the ROIs. Notably, we observed a strong increase of myeloid cells (neutrophils, Mo/Mϕ and dendritic cells) from 4% in controls to almost 28% at day 4 in the imaged ROIs, indicating ubiquitous infiltration of myeloid cells into the infarct (Extended Data Fig. 3b). A deeper analysis of immune cell types allowed classification of neutrophils, different types of Mo/Mϕ as well as lymphoid cells and dendritic cells (Extended Data Fig. 3c,d). Overall, our analysis highlights the cellular landscape of acute MI, recapitulating many known cellular dynamics in a spatial context.

https://doi.org/10.1038/s44161-025-00717-y

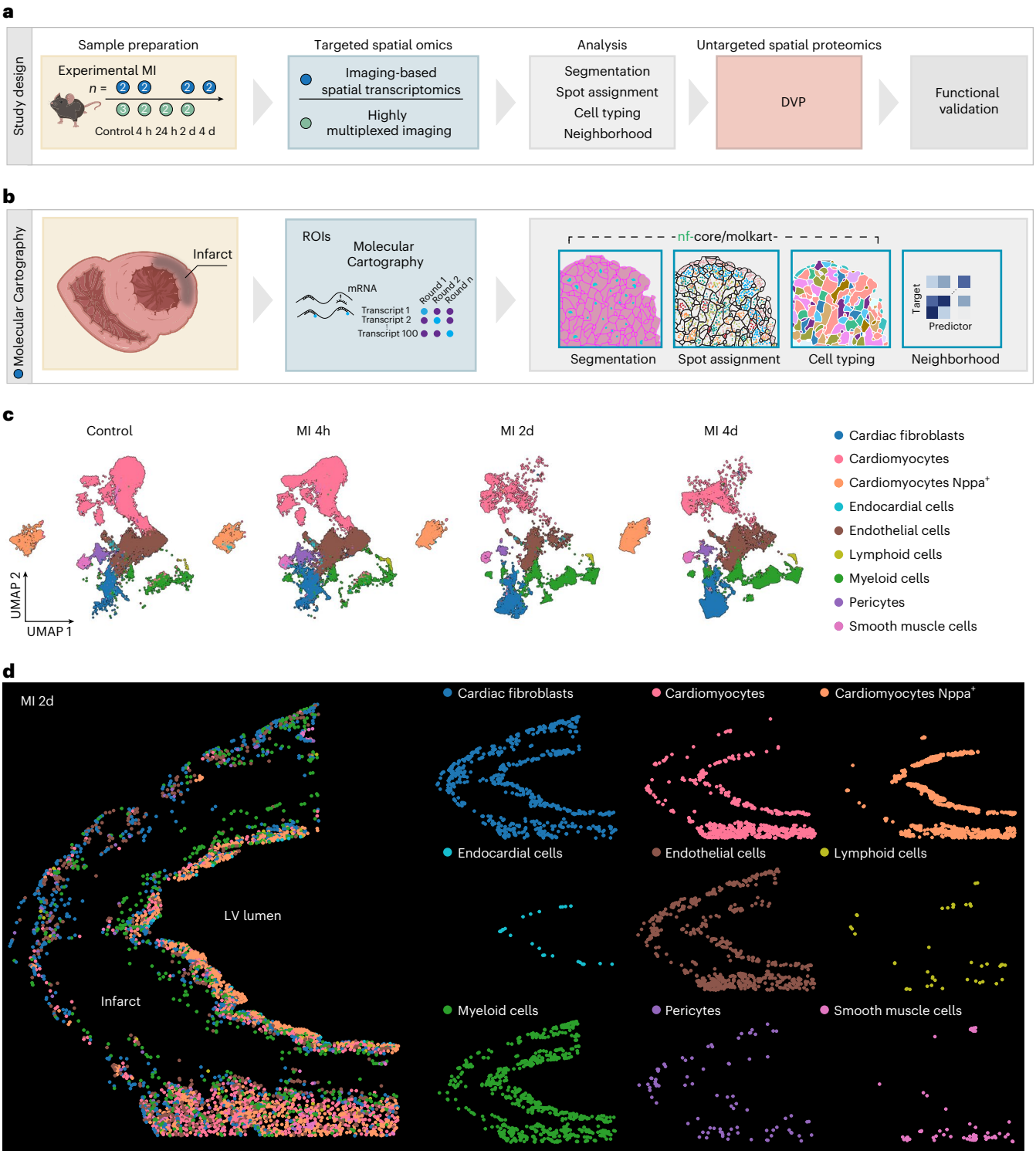

Fig. 1 | Molecular Cartography of acute MI enables spatial cell typing of the left ventricular infarct tissue. a, Schematic overview of the study design. Two biological replicates chosen across two technical replicate slides were used for Molecular Cartography. Two or three biological replicates were used for SeqIF. **b**, Schematic for spatial transcriptomics data generation (Molecular Cartography) and processing (nf-core/molkart). **c**, UMAP showing the joint embedding of 69,028 cells from eight samples (two biological replicates per timepoint) over four timepoints across acute MI. **d**, Representative spatial cell type distributions for a sample at 2 days after MI. A composite image with all cell types is shown on the left, and each cell type's individual distribution is shown on the right. Schematics in **a** and **b** were created with BioRender.com. d, days; h, hours; LV, left ventricular.

Cellular neighborhood analysis of spatial transcriptomic data highlights the dynamic spatiotemporal changes during acute MI

To get a global understanding of the tissue architecture and intercellular relationships across acute MI tissues, we applied the Multiview Intercellular SpaTial (MISTy) modeling framework to our dataset[43]. MISTy captures the cell type relationship patterns across entire slides and datasets in an unbiased manner (Methods). In homeostatic cardiac control tissue, the majority of cell types were distributed mostly

https://doi.org/10.1038/s44161-025-00717-y

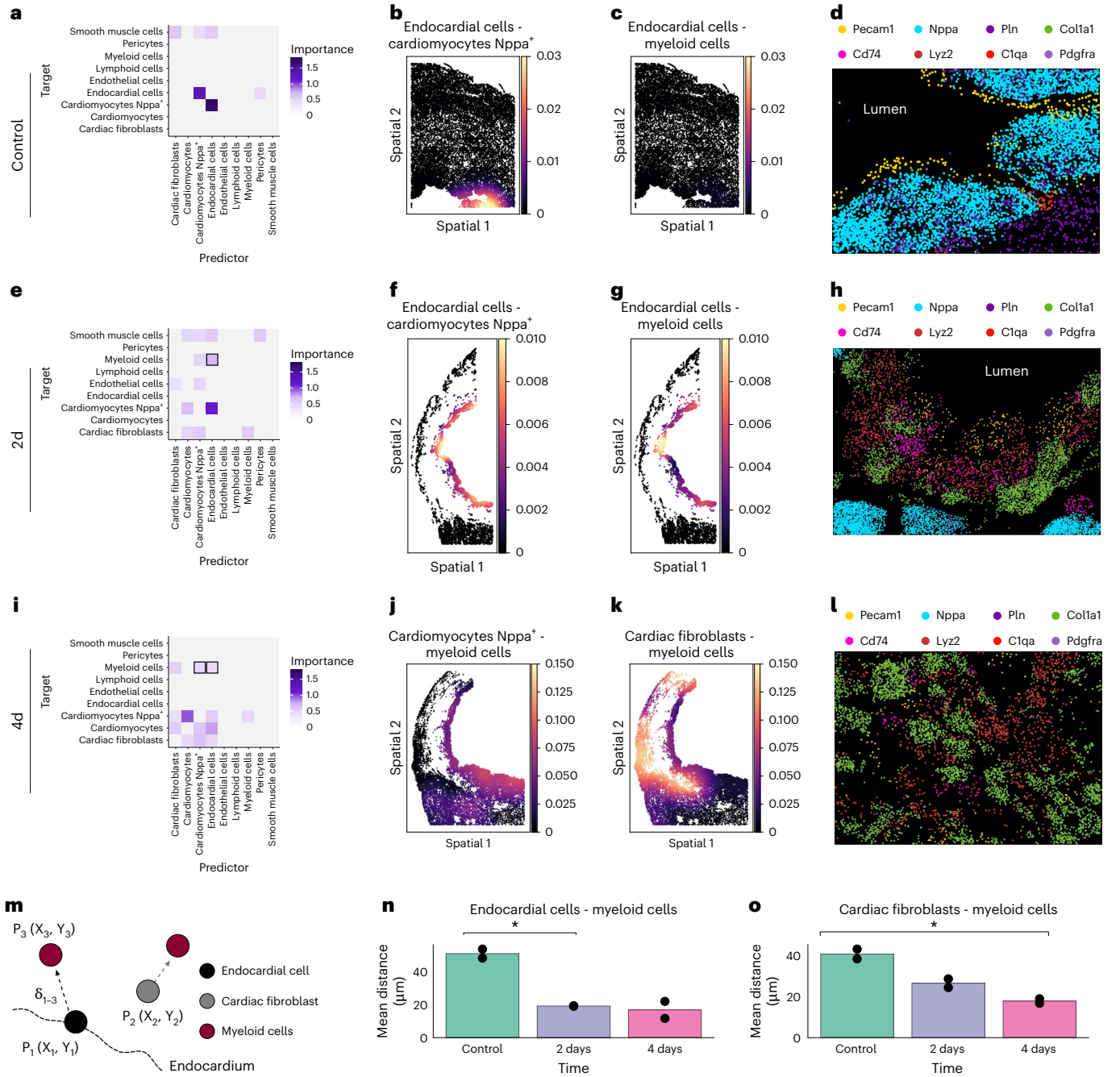

Fig. 2 | Spatial analysis of Molecular Cartography cell composition during MI highlights myeloid interactions with the endocardial layer. a, Spatial cell type relationships in cardiac control tissue as calculated by MISTy. Importance indicates spatial interactions across the slide between the two cell types highlighted. For all MISTy analyses, only interactions with an importance >0.4 and only cell types with a gain in $R^2 > 5\%$ are shown. R^2 represents the change of variance when including the spatial context (paraview, radius = 125 µm). **b**,**c**, Local bivariate analysis between endocardial cells and cardiomyocytes Nppa$^+$ (**b**) and endocardial cells and myeloid cells (**c**), respectively. Color indicates the local product as calculated by LIANA+. **d**, RNA spot localization in an endocardial region of control tissue, highlighting spatial co-localization of marker genes for endothelial/endocardial cells (Pecam1), cardiomyocytes (Pln and Nppa), fibroblasts (Pdgfra and Col1a1) and myeloid cells (Cd74, Lyz2 and C1qa). **e**, MISTy analysis for left ventricular tissue 2 days after MI shows an interaction between endocardial cells and myeloid cells. **f**,**g**, Local interaction analysis shows the interaction of endocardial cells with cardiomyocytes Nppa$^+$ (**f**) and myeloid cells (**g**) in the endocardial infarct zone. **h**, RNA marker expression confirming localized expression of myeloid markers in the endocardial infarct zone. **i**, MISTy analysis for 4 days after MI highlights the spatial relationship between cardiac fibroblast and myeloid cells around the infarct core. **j**,**k**, Local interaction analysis shows the interaction of myeloid cells with cardiomyocytes Nppa$^+$ (**j**) and cardiac fibroblasts (**k**). **l**, RNA spot localization within the infarct tissue at 4 days after MI. **m**, Euclidean distances between all pairs of cell types were calculated. Euclidean distances between all pairs of cell types were calculated and the distance to the closest myeloid cell was used for endocardial cells and cardiac fibroblasts. **n**, Euclidean distances between endocardial cells to myeloid cells were significantly different across the first 4 days after MI ($n = 2$ biological replicates for all groups, type II ANOVA $P = 0.0095$). Post hoc analysis showed significant differences at 2 days (post hoc t-test with Bonferroni correction, $P = 0.022$ after MI relative to control but no difference between 2 days and 4 days ($P = 0.084$)). **o**, Euclidean distances between cardiac fibroblasts and myeloid cells were significantly reduced at 4 days after MI ($n = 2$, same biological samples as in **n**, post hoc t-test with Bonferroni correction, $P = 0.038$). Bars represent mean distance in micrometers, and points represent individual measurements. d, days.

homogeneously, with cardiomyocytes interspersed with cardiac fibroblasts, vascular endothelial cells and pericytes. The location of the majority of cell types was, therefore, not informative as a predictor of the localization of other cell types. MISTy did, however, identify a spatial signature for Nppa$^+$ cardiomyocytes, whose spatial localization was best predicted by endocardial cells (Fig. 2a). Myeloid cells in control tissue were rare, with a relatively homogeneous distribution across the tissue during homeostasis and 4 hours after MI, indicating that these are likely resident leukocytes. To further explore the potential co-localization and interaction between cell types, we performed local, bivariate analysis between pairs of cell types using LIANA+ (ref. 44). This local analysis between endocardial cells and Nppa$^+$ cardiomyocytes in controls pinpointed the interaction between these cell types to the subendocardial region close to the left ventricular lumen (Fig. 2b). This aligns well with known localization of Nppa in trabecular ventricle regions during development, which is maintained in homeostatic adult hearts[45–47]. By contrast, no spatial interaction was identified between myeloid cells and endocardial cells in controls (Fig. 2c). Visualization of the RNA signal within that region confirmed strong Nppa expression close to markers for endocardial/endothelial cells (Pecam1) (Fig. 2d). Two days after MI, MISTy analysis revealed interactions that were not identified in control conditions. Besides the remaining strong relationship between endocardial cells and Nppa$^+$ cardiomyocytes, MISTy also identified a spatial context between endocardial cells and myeloid cells (Fig. 2e). Both of these spatial interactions showed clear demarcation of a (sub)endocardial infarct zone around the infarct core (Fig. 2f,g). In line with this finding, we observed a strong RNA signal of myeloid markers within the endocardium and the subendocardial layers (demarcated by Nppa) (Fig. 2h). The local relationship between endocardial cells and myeloid cells was also identified at 4 days after MI alongside a signal between cardiac fibroblast and myeloid cells (Fig. 2i). Myeloid cell locations at 4 days after MI were additionally predicted by Nppa$^+$ cardiomyocytes, cardiac fibroblasts and cardiomyocytes (Fig. 2j). Interestingly, the interaction between myeloid cells and fibroblasts was enriched in the border zone and epicardial infarct zone (Fig. 2k). The highly increased abundance of cardiac fibroblasts and their spatial co-localization with myeloid cells were further highlighted by the drastic increase of RNA molecules encoding ECM components such as Col1a1 (Fig. 2l). As multiple spatial analyses highlighted unexpected but potentially important interactions between endocardial cells and myeloid cells, we aimed to validate and quantify this increased local relationship using simple measures. Therefore, we calculated the Euclidean distance in two-dimensional tissue space between each endocardial cell and its nearest neighbor myeloid cell to quantify myeloid cell proximity to endocardial cells during acute MI (Fig. 2m). Average distances between endocardial cells and myeloid cells showed significant differences over the MI timecourse (Fig. 2n). At day 2 and day 4 after MI, endocardial cells showed significantly shorter distances to myeloid cells compared to the control, whereas the average distance to myeloid cells did not change significantly between day 2 and day 4 (Fig. 2n). We performed the same distance analysis to see whether myeloid cells show a similar relationship with cardiac fibroblasts at the interface to the infarct core and found increased proximity between both cell types after MI (Fig. 2o). Taken together, our cellular neighborhood analysis identified and highlighted an unexpected spatial relationship between endocardial cells and myeloid cells, suggesting that immune infiltration to the infarct might be mediated via the endocardium and the subendocardial Nppa$^+$ infarct zone (collectively referred to as endocardial infarct zone).

Highly multiplexed antibody-based imaging confirms immune cell infiltration via the endocardial layer in acute MI

To further investigate the regional distribution of myeloid cells after MI and capture spatial temporal patterns across entire heart sections, we performed SeqIF on samples from the acute phase after MI, independent of Molecular Cartography samples (control in biological triplicate; 4 hours, 24 hours and 2 days in biological duplicate) (Fig. 3a)[48]. We optimized an antibody panel to identify healthy and stressed cardiomyocytes (Tnnt2 and Ankrd1), endothelial cells (CD31), smooth muscle cells (αSMA), cardiac fibroblasts (Pdgfra), myeloid cells (CD45, CD68, CCR2, Trem2 and Mpo) as well as DAPI and wheat germ agglutinin (WGA) to capture nuclei and the cell membrane, respectively (Fig. 3b and Supplementary Table 2). We performed image processing of SeqIF data using MCMICRO, a Nextflow-based pipeline that performs subtraction of autofluorescence signal from each antibody channel, cell segmentation and fluorescence intensity quantification (Fig. 3a)[49]. Based on our experience with segmentation for Molecular Cartography data, we applied the same strategy of using WGA and DAPI to train a custom Cellpose 2 model to segment cells in the SeqIF dataset. To assign phenotypes to cells, we used the Pixie workflow, which performs pixel clustering using self-organizing maps (SOMs) to generate pixel maps of tissues (see Methods for more details) (Extended Data Fig. 4a)[50]. In these pixel maps, groups of pixels with similar marker intensity profiles across the SeqIF dataset are clustered together, allowing for classification of different cell types and tissue regions across the entire timecourse of acute MI (Extended Data Fig. 4b)[50]. In line with our results from Molecular Cartography, we found a continuous decrease in pixel phenotype clusters for cardiomyocyte marker Tnnt2 and an increase in pixel phenotype clusters for myeloid cells (Mo/Mϕ and neutrophils) in the first 2 days after MI (Extended Data Fig. 4b,c). We also found stressed and dying cardiomyocytes positive for an Ankrd1 pixel cluster, clearly demarcating the infarct core starting already at 4 hours after MI (Extended Data Fig. 4a). We used the pixel maps to perform cell phenotyping using Cellpose cell masks in a second clustering step (Fig. 3c,d and Extended Data Fig. 4d). This pixel-level phenotyping workflow enabled us to profile the spatial localization of cardiac cells within the infarcted heart based on our highly multiplexed imaging data, at an unprecedented scale for entire heart cross-sections. To further investigate and independently validate the potential relationship between endocardial and myeloid cells that we found in Molecular Cartography data, we repeated the distance analysis between these two groups of cells. In line with our findings with Molecular Cartography, the distance between myeloid cells and endocardial cells decreased during the first 2 days after MI (Fig. 3e). Interestingly, myeloid cells were closest to endocardial cells only 24 hours after an infarct (median distance = 24 µm), suggesting that attachment and infiltration of these immune cells via the endocardial layer might be a rapid process. To quantify the extent of different infiltration routes of myeloid cells into the infarct, we partitioned the infarcted heart images into regional compartments (endocardial infarct zone, epicardium, infarct core and border zone) guided by expression patterns of Tnnt2, Ankrd1, WGA and CD31 (Methods) with subsequent cell quantification (Fig. 3f, Supplementary Figs. 2 and 3 and Extended Data Fig. 5a). Using SeqIF and conventional immunofluorescence staining, we found a strong increase specifically for Mo/Mϕ expressing CCR2 (CCR2$^+$ Mo/Mϕ) in the endocardial infarct zone, peaking at 24 hours after MI (Fig. 3g and Extended Data Fig. 5). At 2 days after MI, the relative number of myeloid cells remained high within the endocardial infarct zone. However, we additionally found an increased density of CCR2$^+$ Mo/Mϕ within the epicardial infarct layer. Quantification of absolute CCR2$^+$ Mo/Mϕ numbers over time identified the border zone as the predominant invasion route after 2 days. Closer inspection of CCR2$^+$ Mo/Mϕ distribution in the endocardial layer showed CCR2$^+$ Mo/Mϕ already being attached to the endocardium at 4 hours after MI, with occasional infiltration events (Fig. 4a–c and Extended Data Fig. 6). Of note, we did not observe a high abundance of non-endocardial endothelial cells in regions with high CCR2$^+$ Mo/Mϕ density within the endocardial infarct zone during the first 24 hours (Extended Data Fig. 6).

In the epicardial layer, CCR2$^+$ Mo/Mϕ were either directly attached to the epicardium or in close proximity to epicardial vessels

https://doi.org/10.1038/s44161-025-00717-y

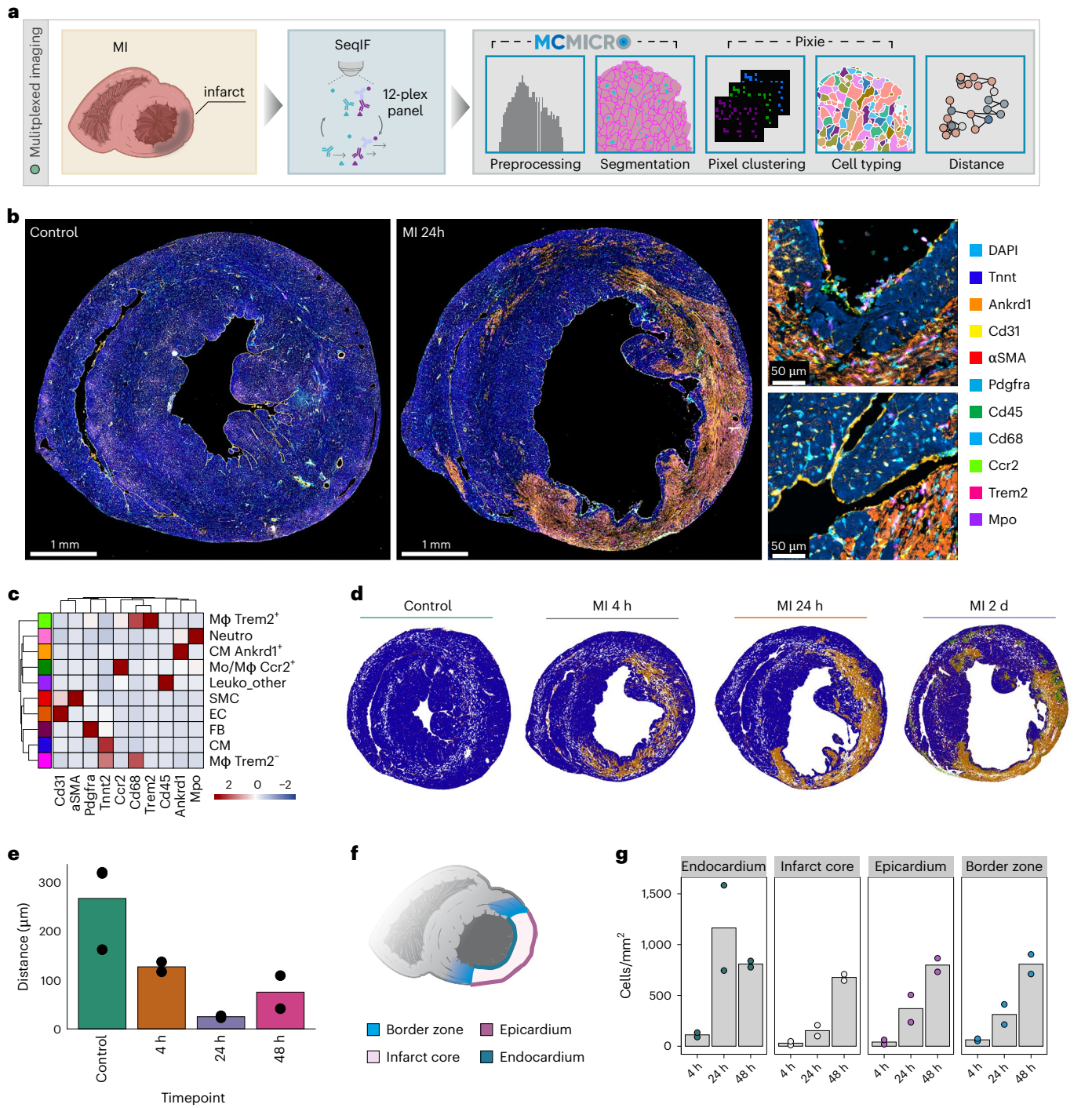

Fig. 3 | Highly multiplexed imaging using SeqIF and conventional immunofluorescence during the first 2 days of acute MI confirms infiltration of myeloid cells via the endocardial layer. a, Schema of experimental design for SeqIF data generation and processing. For SeqIF, three biological replicates were sampled for controls and two biological replicates for the remaining timepoints. All SeqIF replicates were different mice than those used for Molecular Cartography experiments. **b**, Representative SeqIF of mouse heart cross-sections using 10 antibodies before (left) and at 24 hours after (right) MI. Magnifications on the right highlight endocardial niches in the infarct, characterized by the presence of stressed cardiomyocytes (Ankrd1$^+$, orange) and attachment of immune cells to endocardial cells (CCR2$^+$ in green, Mpo$^+$ in violet and CD31 in yellow). ROIs, 50 µm. **c**, Cell phenotyping heatmap from Pixie highlighting marker expression in different cell masks across the entire dataset. Legend represents the scaled marker expression, which was capped at 3. **d**, Pixie cell phenotyping for one representative sample per timepoint. Each pixel is colored based on its cell pixel cluster as calculated by Pixie. Cell type colors correspond to heatmap grouping colors in **c**. **e**, Distances in micrometers from endocardial cells to the closest myeloid cell quantified at four different timepoints from SeqIF images. Distances show a significant change across the measured timepoint ($n = 2$ biological replicates for all timepoints, type II ANOVA $P = 0.0279$). Bars show mean distances across biological replicates, and points represent mean distances per biological replicate. **f**, Schema of anatomical annotations used to calculate myeloid cell infiltration. **g**, Quantifications of Ccr2$^+$CD68$^+$ Mo/Mϕ in different spatial regions in cross-sections from SeqIF. Relative cell type abundance is visualized as cells per mm^2. Bars show mean abundance, and points represent individual measurements from biological replicates ($n = 2$ for each timepoint). Schematics in **a** and **f** were created with BioRender.com. CM, cardiomyocyte; d, days; EC, endothelial cell; FB, fibroblast; h, hours; Leuko, leukocyte; SMC, smooth muscle cell.

https://doi.org/10.1038/s44161-025-00717-y

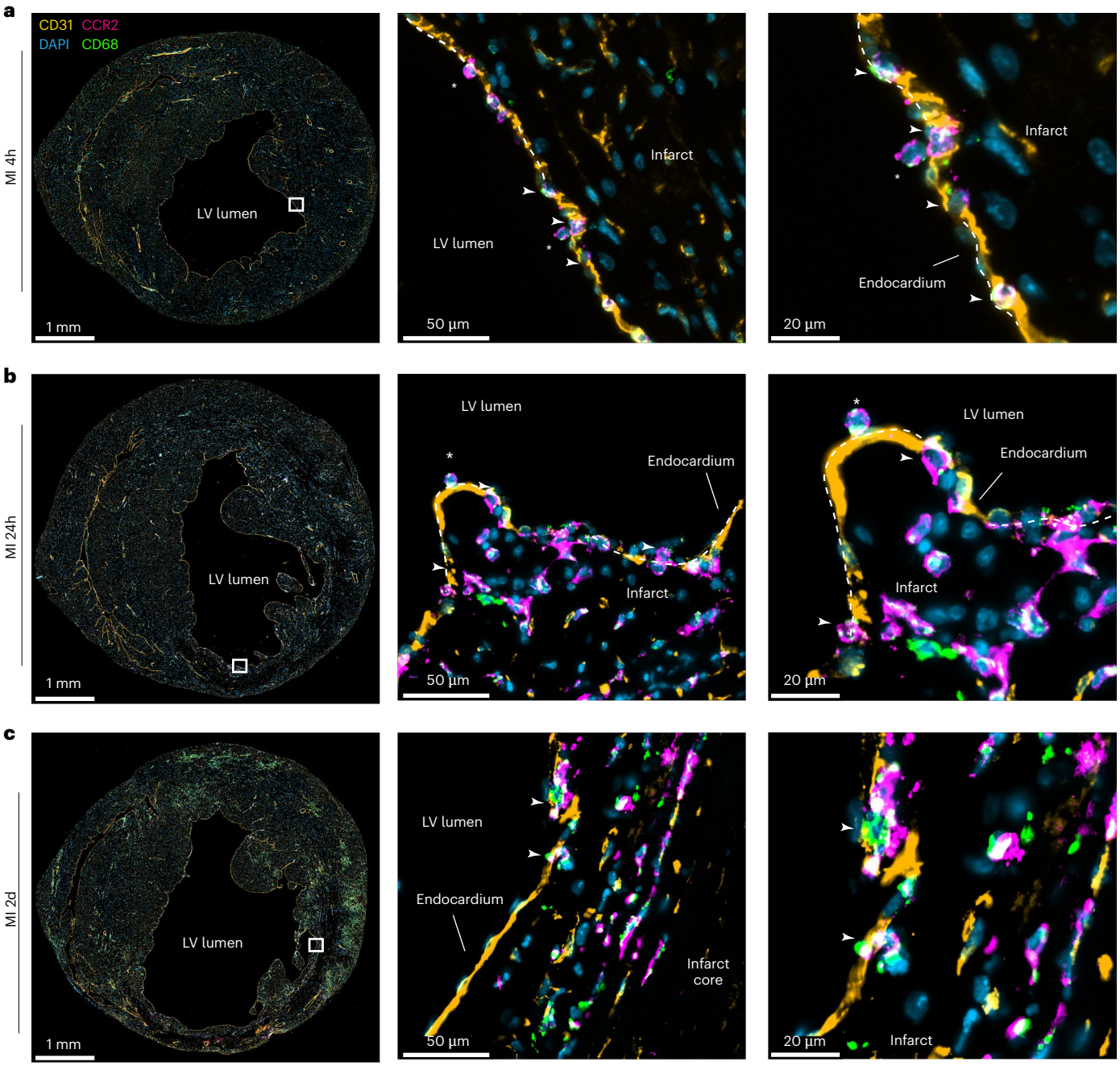

Fig. 4 | Mo/Mϕ infiltrate the infarcted heart via the endocardium. **a**–**c**, Representative SeqIF stainings showing selected markers, including CD31 (yellow), CCR2 (magenta), CD68 (green) and DAPI (blue). Staining of sections 4 hours (**a**), 24 hours (**b**) and 2 days (**c**) after MI indicates increased attachment (asterisk) and transmigration (arrow), resulting in high density of $CCR2^{+}CD68^{+}$ cells in the (sub)endocardial infarct zone and movement of $CCR2^{+}$ cells toward the infarct core. Mid and right panels represent magnifications of the marked box in the left overview panel. d, days; h, hours; LV, left ventricular.

(Supplementary Fig. 4a–c). Taken together, our results—across multiple technologies and quantification methods—clearly indicate a progressive infiltration of myeloid cells via different cellular layers during the acute phase after MI in a non-reperfusion context and highlight a previously undescribed route via the endocardial infarct zone that immune cells can take to infiltrate the left ventricle to reach the infarct region.

Spatial proteomics of the endocardial layer highlights vWF involvement in immune cell infiltration

Following the discovery of early immune cell infiltration into the endocardial infarct zone, we aimed to identify potential factors mediating the recruitment, adhesion and infiltration of myeloid cells via the endocardium using ultrasensitive mass spectrometry-based proteomics[36]. Therefore, we used laser capture microdissection to excise the endocardial region from healthy mouse hearts (control) and hearts 24 hours after MI. For hearts with MI, we split endocardial cells into two groups: those that were within the infarct zone (MI IZ) and those that were remote to the infarct (MI remote) (Fig. 5a). Proteomes of the different endocardial tissue samples encompassed an average number of 3,274 proteins after quality control filtering (Supplementary Fig. 5a). Despite the very low amount of input tissue material, the proteomic data were of high quality with a low amount of missing protein values (4–16% across samples) (Supplementary Fig. 5b). PCA of proteomic

https://doi.org/10.1038/s44161-025-00717-y

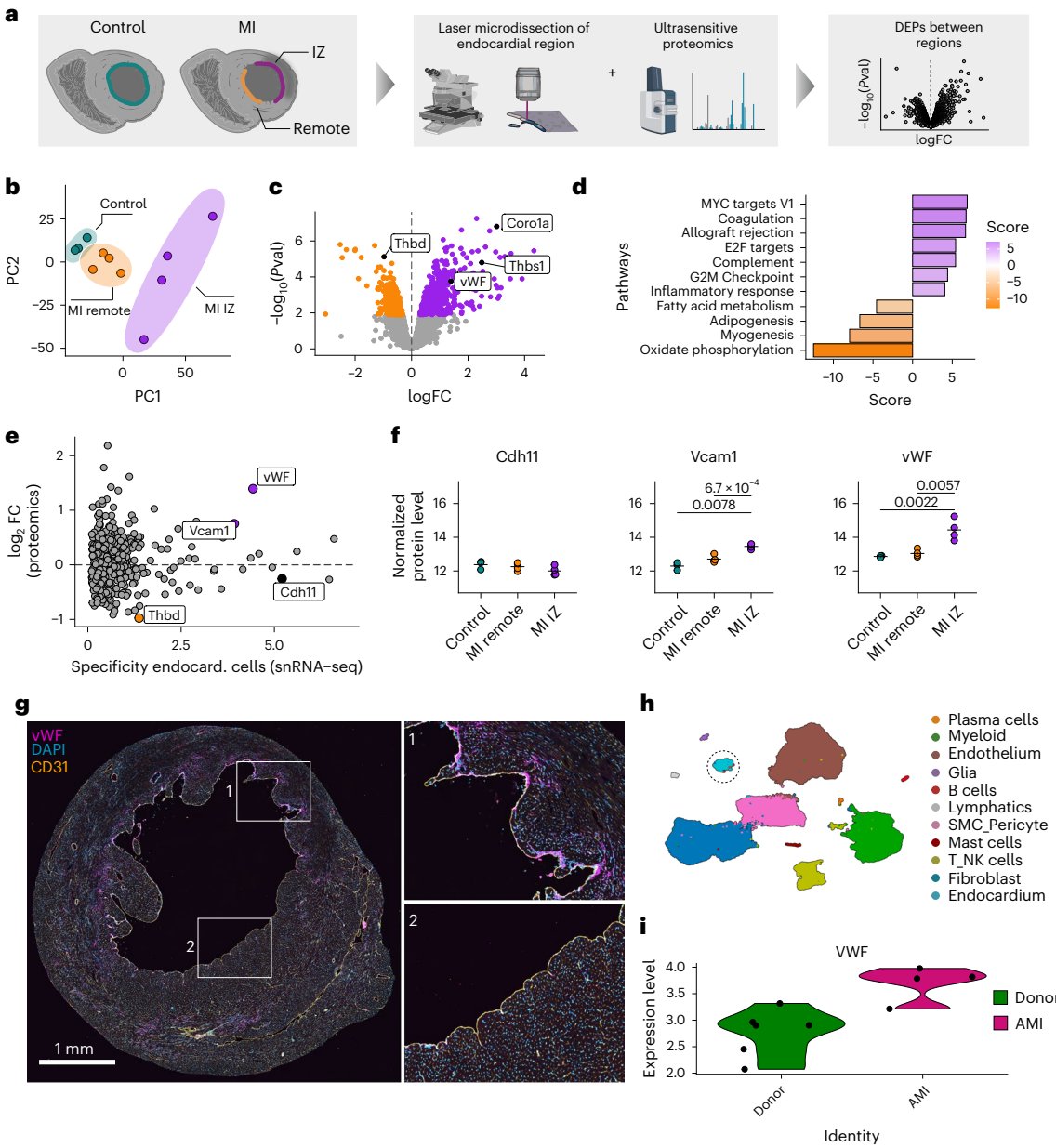

Fig. 5 | Laser capture microdissection coupled to ultrasensitive proteomics at 1 day after MI reveals local vWF upregulation in endocardial cells. a, Schema for experimental design comparing endocardium of control (green), infarct zone (IZ, purple) and remote regions (orange). **b**, PCA of the three indicated experimental groups ($n = 3–4$ biological replicates). **c**, Volcano plot of the proteomic differential comparison between infarct endocardium and remote endocardium. Significantly differentially expressed proteins are displayed in purple (upregulated in infarct endocardium) and orange (downregulated in infarct endocardium). Differential expression was assessed by an empirical Bayes moderated *t*-test (limma-voom). **d**, Pathway enrichment analysis results using hallmark gene sets of DEPs between MI IZ and MI remote. **e**, Endocardial cell specificity analysis of DEPs between MI IZ and MI remote. The *x* axis shows specificity of gene expression (as approximated by differential marker gene expression) based on snRNA-seq data from Calcagno et al.[22], whereas the *y* axis shows $\log_2$FC from differential protein expression analysis shown in **c**. **f**, Expression plots of three proteins of interest based on ultrasensitive proteomics. Cdh11 is a marker for endocardial cells and not differentially expressed, whereas Vcam1 and vWF show significant differential expression during acute MI ($n = 3$ for control and $n = 4$ for MI remote and MI IZ groups; *P* values shown are from differential expression assessed by an empirical Bayes moderated *t*-test (limma-voom)). Line represents mean expression, and points represent individual measurements. **g**, Representative conventional immunofluorescence staining of vWF (magenta) alongside CD31 (yellow) 24 hours after murine MI. **h**, UMAP of human cardiac cell types identified in snRNA-seq data from Amrute et al.[52]. Endocardial cell cluster used for differential gene expression analysis is highlighted with a dotted circle. **i**, Violin plot of normalized RNA expression from snRNA-seq data aggregated to pseudobulk for all donor samples ($n = 6$) and acute MI samples ($n = 4$) from Amrute et al.[52], with significant upregulation of vWF in human endocardial cells of acute MI samples (DESeq2 analysis on pseudobulk expression values; $P = 1.4 \times 10^{-5}$). Schematic in **a** was created with BioRender.com. AMI, acute MI; FC, fold change; NK, natural killer; PC, principal component; *P*val, *P* value.

samples showed clear separation of control endocardial samples compared to endocardial cells from infarcted samples, indicating a reproducible perturbation of the endocardial layer protein signature 24 hours after MI (Fig. 5b and Supplementary Fig. 5c). Interestingly, the remote endocardial layer signature from infarcted hearts (MI remote) was sufficiently different from control endocardial cells to distinguish

https://doi.org/10.1038/s44161-025-00717-y

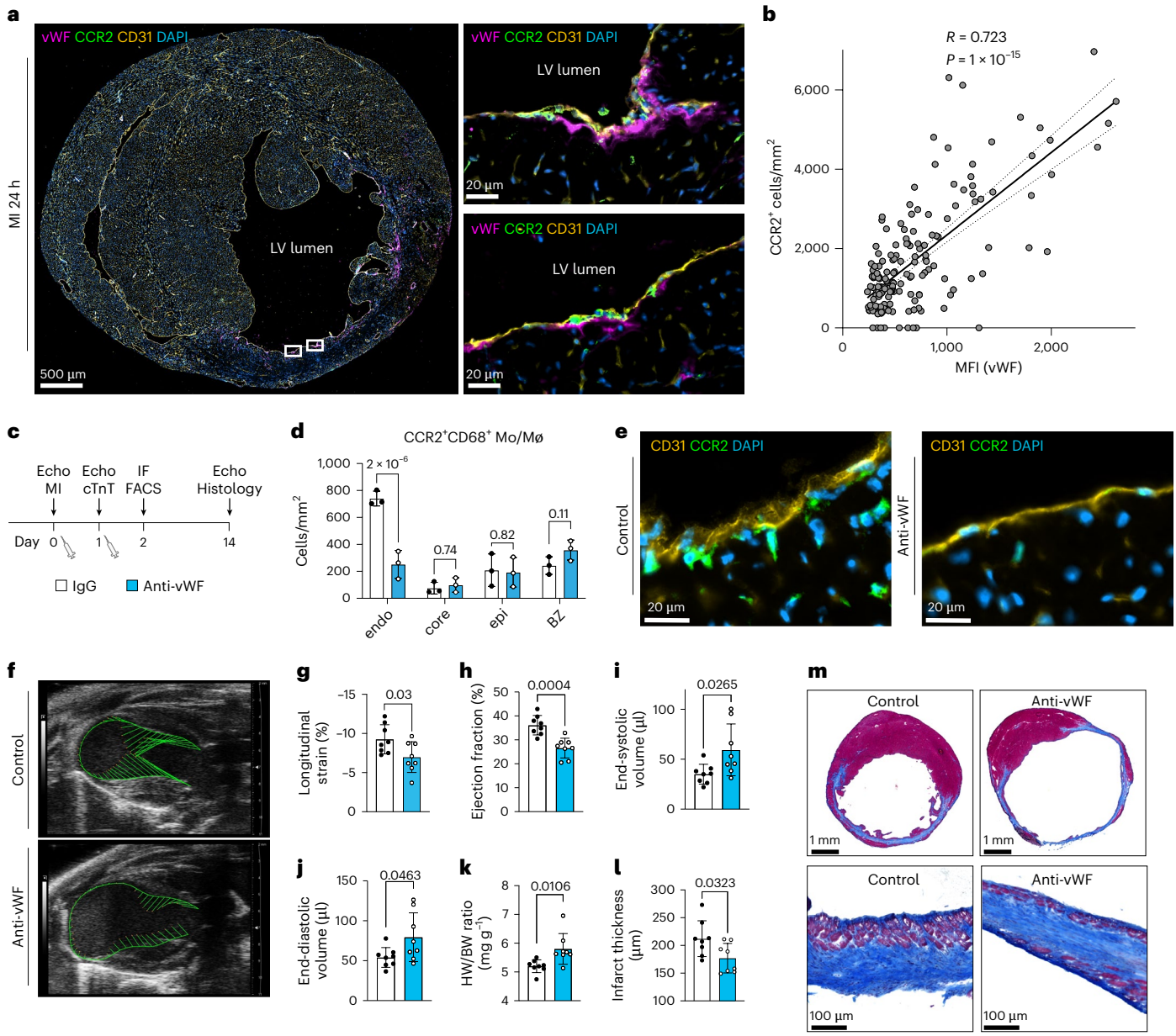

Fig. 6 | Blockade of vWF results in decreased Mo/Mϕ recruitment and impaired infarct healing. a, Representative immunofluorescence staining of vWF, CCR2, CD31 and DAPI 24 hours after MI. **b**, Correlation of CCR2$^+$ cells and mean fluorescence intensity (MFI) of vWF within the endocardial infarct area. A total of 164 annotations of similar size were added across the endocardium to assess vWF MFI and the presence of CCR2$^+$ cells within each annotation ($n = 3$ samples; dashed lines indicate 95% confidence intervals). *R* represents the correlation coefficient. **c**, Schema of the experimental setup for functional vWF blocking during acute MI. **d**, Quantitative analysis of cardiac Mo/Mϕ 2 days after MI based on conventional immunofluorescence in different regions (BZ, border zone; core, infarct core; endo, endocardial IZ; epi, epicardial IZ). Boxes represent mean ± s.d. ($n = 3$ samples per group). *P* values were determined by two-way ANOVA followed by Sidak's multiple comparison. **e**, Representative immunofluorescence stainings of CCR2$^+$ cells (green) after both IgG and anti-vWF treatment 2 days after MI in the endocardial IZ. **f**, Representative B-mode images 14 days after MI induction. Green lines depict left ventricular endocardial displacement. **g**–**j**, Global longitudinal strain (**g**), left ventricular ejection fraction (**h**) and end-systolic (**i**) and end-diastolic volume (**j**) determined by echocardiography 14 days after MI induction. **k**, Heart weight (HW) to body weight (BW) ratios after organ removal 14 days after MI. **l**, Quantification of infarct thickness based on histopathological evaluation 14 days after MI. Data show mean ± s.d.; points display individual measurements ($n = 8$ samples per group). *P* values were calculated using two-tailed Student's *t*-test. **m**, Representative images of Masson trichrome stainings of both IgG-treated and anti-vWF-treated mice 14 days after infarction. h, hours; IF, immunofluorescence; LV, left ventricular.

them in the PCA, but there were very few significantly differentially expressed proteins (DEPs) between these two conditions (Supplementary Fig. 5d). By contrast, significant differential protein expression of many proteins was observed in the endocardial region in the infarct zone (MI IZ) relative to the remote endocardial region (MI remote) (Fig. 5c). Pathway analysis using hallmark gene sets of DEPs between MI IZ and MI remote revealed upregulated pathways related to immune cell activation (complement system, inflammatory response and IFNγ response) as well as downregulated pathways related to energy metabolism (oxidative phosphorylation and fatty acid metabolism) (Fig. 5d). Interestingly, we identified genes for coagulation pathways strongly upregulated in MI IZ samples relative to MI remote regions (Fig. 5d). We investigated the cell specificity of these pathway results using a published snRNA-seq dataset and found vWF as the most specific

endocardial protein that was significantly upregulated in MI IZ compared to MI remote, similar to known endothelial adhesion molecules such as Vcam1 (Fig. 5e,f)[22]. vWF is a multimeric protein that plays a central role in vascular homeostasis and is involved in inflammatory processes[51]. Interestingly, vWF was not significantly upregulated in the remote endocardial regions of infarcted hearts (MI remote) compared to endocardial regions of control hearts (Fig. 5f). To confirm increased localization of vWF proteins in the endocardial infarct zone, we performed conventional immunofluorescence staining of vWF in infarcted hearts and found a significantly stronger signal in the endocardial infarct area, with an almost absent signal in the remote region (Fig. 5g and Extended Data Fig. 7a,b). The distribution of vWF$^+$ staining, interestingly, was not uniform across the infarct adjacent endocardial layer but stronger at endocardial sites where the ventricular tissues formed pockets, compared to smooth regions. Immunofluorescence stainings of murine hearts 24 hours after ischemia/reperfusion injury also showed similar staining patterns with increased vWF expression (Extended Data Fig. 7c,d). To investigate whether vWF also plays a role in human MI, we reprocessed a cellular indexing of transcriptomes and epitomes by sequencing (CITE–seq) dataset of explanted human hearts from donors and patients with acute MI by Amrute et al. [52] (Fig. 5h). This dataset consists of healthy donors, patients with acute MI and patients with chronic ischemic and non-ischemic cardiomyopathy, from which we focused on healthy donors ($n = 6$) and patients with acute MI ($n = 4$). Differential gene expression analysis demonstrated a significant increase of endocardial vWF expression in patients after acute MI compared to healthy donors (Fig. 5i). Collectively, our DVP analysis during acute MI revealed local spatial differences between endocardial regions within the same heart and highlighted upregulation of vWF as a specific response of the endocardium to the local inflammatory signals from the infarct zone.

Functional blocking of vWF modifies immune cell infiltration and infarct recovery

Immunofluorescence co-staining of CCR2 and vWF highlighted a strong correlation between the presence of vWF within the endocardial infarct region and locally attached or already infiltrated CCR2$^+$ Mo/Mϕ after MI and myocardial ischemia/reperfusion (Fig. 6a,b, Extended Data Fig. 7d,e and Supplementary Fig. 6a,b). Of note, immunofluorescent co-staining of platelets revealed their presence in some, but not all, of these infiltration areas with expression of vWF (Supplementary Fig. 6c). We conclude that vWF-dependent immune recruitment in this context is, at least partially, platelet independent. To investigate the functional role of vWF in the recruitment and infiltration of myeloid cells via the endocardium during acute MI, a well-characterized polyclonal antibody (against human vWF, which is also highly cross-reactive with murine vWF) was used to block vWF function in murine MI (Fig. 6c)[53–55]. Under baseline conditions, anti-vWF blockade led to no cardiac-specific phenotype in healthy mice (Supplementary Fig. 7a–d). Control IgG or anti-vWF antibodies were injected intravenously at 0 hours and 24 hours after MI. Blockade of vWF resulted in a significant decrease in recruited Mo/Mϕ in the infarcted myocardium as quantified by flow cytometry 2 days after MI, whereas blood levels of Mo/Mϕ were unaltered (Supplementary Fig. 7e,f). Immunofluorescence staining demonstrated that this effect was mainly explained by dramatically reduced Mo/Mϕ within the endocardial infarct zone (Fig. 6d). Interestingly, blockade of Mo/Mϕ recruitment mediated by vWF blocking at the endocardium led to impaired healing and deteriorated long-term outcome 2 weeks after MI induction as shown by echocardiography (Fig. 6f–j). Moreover, histopathological evaluation revealed more pronounced infarct thinning in anti-vWF-treated mice compared to control mice (Fig. 6k–m). Our findings using DVP and functional experiments have, therefore, uncovered a potentially critical role of the endocardium in facilitating infiltration of myeloid cells that is likely mediated by vWF.

Discussion

This study reveals a previously undescribed route for immune cell infiltration of monocytes during the acute phase of MI in mice. Using a combination of state-of-the-art spatial omics approaches such as Molecular Cartography, SeqIF and DVP, we identified the endocardium as an important region of immune cell attachment and infiltration, mediated by the local upregulation of vWF.

A wide range of clinical trials are currently testing the potential of immunomodulation to prevent adverse remodeling after MI. A better mechanistic understanding of leukocyte accumulation and the differentiation of beneficial and harmful players in this context might lead to novel and improved strategies to improve MI healing. High-resolution spatial assays allowed us to observe and identify the attachment and infiltration of myeloid cells through the endocardial layer of the left ventricle during the critical early timeframe of acute MI. Over time, the healing heart appears to develop different hubs of local inflammation: early on, a large number of monocytes accumulate via the endocardial layer and, at later stages, with a dominant and well-described focus in the border zone. Depending on the timepoint, it should also be considered that additional infiltration might occur via the subendocardial microvasculature. Although most experiments were carried out after permanent coronary occlusion, we also observed this effect in the context of cardiac ischemia/reperfusion.

The central mediator for the attachment of monocytes in the lumen of the left ventricle was identified to be vWF, released from endocardial cells in the infarct zone. vWF is known to be involved in platelet adhesion and aggregation, and, although we did observe some vWF cell clusters with platelets present, many myeloid cell–endocardial cell interactions occurred in the absence of platelets, suggesting that the vWF effect on immune cell infiltration is at least partially platelet independent[56]. The in vivo blockade of vWF resulted in a significant reduction in subendocardial monocyte accumulation. Recent studies suggest that vWF can have direct effects on immune cells, independent of platelets[57]. vWF might not only impact migratory capabilities but might also modify their pro-inflammatory activation or shift macrophage metabolism toward glycolysis in a p38-dependent manner. Although we did not observe any hemorrhage or other signs of bleeding in the treated animals, blockade of vWF might also affect primary hemostasis and, thereby, impact monocyte accumulation subsequently. The observed effect that a reduced accumulation of CCR2$^+$ monocytes (by vWF blockade) results in impaired left ventricular function was surprising and could indicate that this particular subset plays a beneficial role in the context of infarct healing and might be distinct from monocyte subsets present in the border zone of the infarcted heart. Whether the route of infiltration or the local micro-milieu instructs the flavor of the myeloid cell remains to be explored.

We observed a localized upregulation of vWF only in endocardial cells within the infarct zone, suggesting potential signaling effects from dying cardiomyocytes and other cells in the spatial neighborhoods of the infarct. It appears that vWF is primarily released from endocardial cells within hypokinetic or akinetic areas of the left ventricle, which could also indicate an impact of altered blood flow on the secretome of this cell layer. Although we do not have any data to confirm these hypotheses, future studies might investigate the signaling molecules reaching endocardial cells and try to isolate which factors are causing the upregulation of vWF.

Although our findings are based on multiple types of experimental approaches, and we consistently observed immune cell infiltration via the endocardial infarct zone regardless of the technology used, our study does have several limitations. First, the transcript panel that we selected for Molecular Cartography is limited to 100 different transcripts and was manually curated and is, therefore, lacking many potentially interesting and important markers for detailed description of immune cell types. Furthermore, some transcripts are not reliably detected with probes that we selected in our target tissue and,

therefore, might observe dropout in cells that do express these RNA, leading to dropout effects. Another limitation we face is the lack of high-quality reference data for cardiac cell segmentation. Although we trained a custom cell segmentation model using Cellpose 2, with as little bias as possible, this segmentation does not represent a real ground truth but solely an approximation. Hopefully, as more high-resolution spatial omics datasets become available, public datasets with representative cardiac cell segmentation masks will become available for future studies.

We attempted additional validations using publicly available data sources to find a signature of endocardial immune cell infiltration during acute MI. Unfortunately, most published studies either do not match the temporal window that is critical to observe this effect or employ spatial methods with insufficient resolution[22,23]. Although we employed cell deconvolution methods on some of these datasets, it was not possible to identify endocardial regions with sufficient sensitivity to validate our findings using such datasets.

In conclusion, our findings of immune cell infiltration via the endocardial infarct zone in acute MI open new and exciting avenues to modulate the immune response after an infarct and provide novel opportunities for therapeutic avenues and drug delivery.

Methods

Mouse experiments

C57BL/6NRj female mice were obtained from Janvier Labs and were studied at 10–12 weeks of age. Mice were housed under standard laboratory conditions with a 12-h light/dark cycle and access to water and food ad libitum. All animal procedures were approved by the institutional review board of the University of Heidelberg, Germany, and the responsible government authority of Baden-Württemberg, Germany (project numbers G-106/19 and G-94/21).

Minimally invasive induction of MI

MI was induced in a minimally invasive manner under echocardiographic guidance[35]. In brief, mice were anesthetized with inhalation of 2% isoflurane and placed on a Vevo imaging station connected to a Vevo 2100 system (VisualSonics). After a brief evaluation of cardiac function, the left coronary artery was visualized. After attaching a neutral electrode, a monopolar needle controlled by a micromanipulator was inserted into the chest and placed on the coronary artery. The vessel was coagulated with high-frequency electricity using an electrosurgical station that was connected to both electrodes. After removal of the needle, successful MI was confirmed by persisting absence of a Doppler signal and akinesia in the affected part of the left ventricular wall. For induction of myocardial ischemia/reperfusion, the left coronary artery was occluded (60 minutes) via two micromanipulator-controlled needles under echocardiography guidance as previously described[58]. Healthy untouched mice showed similar Mo/MΦ levels in the myocardium compared to sham-treated mice and were, therefore, used as biological controls (Supplementary Fig. 8).

Organ removal and preparation

Peripheral blood was collected by facial vein puncture in heparinized tubes. Hearts were excised after cervical dislocation and rinsed extensively in ice-cold PBS to remove remaining blood within the left ventricular lumen and vasculature. After transverse sectioning using a scalpel, freshly dissected mouse cardiac samples were embedded in Tissue-Tek Optimal Cutting Temperature (OCT) compound (Sakura) in a plastic cassette and were immediately placed in an isopentane bath on dry ice for further processing.

Molecular Cartography (highly multiplexed smFISH) of murine MI samples

Next, 10-µm-thick cryosections were placed within the capture areas of cold Resolve Biosciences slides. Samples were sent to Resolve Biosciences on dry ice for analysis. Upon arrival, mouse tissue sections were thawed and fixed with 4% v/v formaldehyde (Sigma-Aldrich, F8775) in 1× PBS for 30 minutes at 4 °C. After fixation, sections were washed three times in 1× PBS for 1 minute, followed by a 1-minute wash in 70% ethanol at room temperature. Fixed samples were used for Molecular Cartography (100-plex combinatorial smFISH) according to the manufacturer's instructions and as previously described[59]. The probes for 100 genes were designed using Resolve Biosciences' proprietary design algorithm. Supplementary Table 1 highlights the gene names and catalog numbers for the specific probes designed by Resolve Biosciences.

Image processing of Molecular Cartography data

Slides used for combinatorial smFISH imaging with Molecular Cartography for 100 candidate transcripts were subsequently stained for nuclei (DAPI) and WGA. DAPI and WGA images as well as RNA spot tables from Molecular Cartography were processed using an in-house-developed Nextflow pipeline: nf-core/molkart (https://doi.org/10.5281/zenodo.10650748, revision: 81eafe9f9993d4daf16371ba3804ce9ae08053ad). The pipeline is part of the nf-core collection of workflows adhering to strict guidelines for best practices in Nextflow workflow development. Many core components of the pipeline were made available as nf-core DSL2 modules to facilitate easy enhancement of the pipeline by other users and to enable reuse of pipeline components by Nextflow imaging pipelines in the future[60]. First, consecutive Gaussian blurring was used to fill in black grid lines from Molecular Cartography imaging using the Python tool MindaGap[61]. Next, image stacks of DAPI and WGA were created, and contrast-limited adaptive histogram equalization (CLAHE) was applied to improve contrast across stainings for automated segmentation[62]. Training images for Cellpose (TIFF format) were created with the use of the 'create training subset' functionality of the nf-core/molkart pipeline. Cell segmentation was performed using several different segmentation algorithms to compare them on cardiac images (Supplementary Fig. 3). The segmentation algorithms used here were DeepCell Mesmer, which performs nuclear and whole-cell segmentation, and Cellpose[33,34,42]. For Cellpose segmentation, we applied the 'cyto' model, but we additionally trained a custom Cellpose 2 model, by selecting small crops (1,000 × 1,000 pixels) of DAPI and WGA image stacks across the entire dataset, using a human-in-the-loop approach, as described by Pachitariu and Stringer[33,34]. We used the baseline model CPx with flow_threshold = 0.6 and cellprob_threshold = 0 to segment an initial image crop, and we corrected wrong segmentations and retrained the model. This process was consecutively applied to retrain the model on new image crops until segmentation captured most cells correctly in the presented image. After segmentation, the resulting masks were size filtered to remove extremely small and extremely large objects that do not represent real cells (below 200 and above 200,000 pixels). To assign spots to cells, spots are first filtered for potential duplicates using the MindaGap duplicatefinder function, which filters potential duplicate RNA spot calls along black grid lines. Deduplicated RNA spots are then assigned to segmentation masks using spot2cell. Finally, quality control metrics of all relevant steps are collected and compiled for inspection via MultiQC. Images and spots were visualized using the napari toolkit, which enables fast and interactive visualization of large imaging data [63].

Single-cell analysis of Molecular Cartography data

Cell-by-feature matrices from nf-core/molkart were imported into R and processed using the Seurat package (version Seurat_5.0.1)[64–67]. We filtered out cells with fewer than 20 and more than 4,000 RNA counts. We also filtered outlier cells based on their segmentation mask shape with extent <0.25 and solidity <0.75 (as estimated by the regionprops_table function from the scikit-image package in Python) to ensure that only high-quality segmented cells are included in the analysis. Cell transcript profile counts were normalized using SCtransform

in Seurat; principal components were calculated; and the first 30 principal components were used for integration of samples across time using the IntegrateLayers function in Seurat with the method set to 'HarmonyIntegration'[65,67–71]. Harmony embeddings were then used for uniform manifold approximation and projection (UMAP) and cluster identification using shared nearest neighbor analysis using the first 30 harmony dimensions. We used cell type label transfer to annotate the Molecular Cartography cells using a reprocessed snRNA-seq reference from Calcagno et al.[22]. To reprocess the snRNA-seq data from Calcagno et al., we performed Seurat analysis on the raw data as described by the authors in the original publication. The transferred labels from Calcagno et al. were used to guide manual annotation of cells into cell types and states and produce final labels for all cell clusters. To improve the annotation of endocardial cells, we additionally manually labeled the endocardial region in all DAPI+WGA images using QuPath[72]. We exported endocardial masks as GeoJSON files in QuPath and processed them using the sf package in R to overlay centroid positions of cell masks. Cells that overlapped the endocardial region and expressed Pecam1 (normalized count >0) or were clustered into an $Npr3^{+}$ cell cluster were considered as endocardial cells. Although Npr3 is primarily expressed in the endocardial cells in our dataset, the absence of detected Npr3 transcripts in a subset of endocardial cells may reflect transcriptional heterogeneity and/or technical limitations of Molecular Cartography in capturing low-abundance transcripts (Supplementary Fig. 9).

We characterized structural patterns in immediate cellular neighborhoods by extracting cell type to cell type relationships with MISTy (R package mistyR, version 1.99.9)[43]. MISTy is a multiview framework for analysis of spatial omics data by identification of robust relationships within the data coming from different spatial contexts. Based on Molecular Cartography-assigned cell types, we represent each cell type intrinsically as a one-hot encoded vector. To capture the structure of the spatial neighborhood of each cell, we added a paraview with a radius of 125 µm. The paraview captures the neighborhood composition by distance-weighted sum of one-hot encoded representation of the cell types in the surrounding of each cell. The weights are calculated by a radial basis function with parameter equation to the chosen radius. Subsequently, a MISTy model was trained using the same view composition for each sample independently. The MISTy models are trained on the task of predicting each intrinsic cell type by using all variables from the paraview. The MISTy output consists of the gain of variance explained per target and importances of each predictor–target interaction. The importance of each interaction was standardized to 0 mean and unit s.d. across all predictors for a given target. The performance and interaction results were aggregated per timepoint and filtered to exclude all targets with gain of variance explained less than 5% and relationships with importances lower than 0.4. MISTy captures robust relationships on a global scale—that is, consistently across the whole slide. Additionally, MISTy can learn not only simple linear relationships but also complex nonlinear relationships. To linearly approximate the sign of the remaining relationships and estimate their consistency across each slide, we calculated the correlation between the predictor variables from the paraview and the target variables from the intraview. Although strong correlations are indicative of linear and consistent relationships, correlations close to 0 point toward nonlinearity or heterogeneity of the form of the interaction across the slide, warranting a more targeted local bivariate spatial analysis. We used LIANA+ (version 1.0.4) to calculate spatially informed local bivariate metrics between pairs of cell types of interest. Similar to MISTy, we used one-hot encoded cell type vectors and calculated the cell neighborhoods using a Gaussian kernel with a cutoff of 0.1 and a bandwidth of 125 µm and l1 standardization of terms. We then use the lr_bivar function in LIANA+ to calculate the normalized weighted product between two cell type vectors as input. Interactions were visualized by plotting local scores on tissue coordinates. To calculate Euclidean distances between pairs of cells, we used the Scipy spatial packages cdist function[73]. Statistical testing on distances was performed with ANOVA with a linear ordinary least squares (OLS) model and post hoc *t*-tests with Bonferroni correction using the statsmodel application programming interface in Python[74].

SeqIF imaging using Lunaphore COMET platform

To establish an antibody panel for SeqIF, we sourced high-quality antibodies from trusted vendors and performed test stainings at the vendor-recommended concentrations on the COMET priority access platform. If staining was too strong or weak, dilution curves were performed, and staining specificity was manually evaluated. Fluorescence signal acquisition in the Cy5 channel demonstrated higher signal-to-noise ratios and overall cleaner results, whereas the TRITC channel exhibited increased autofluorescence. Of the 16 antibodies initially selected, 12 were imaged in the Cy5 channel due to the predominance of functional antibodies raised in rabbit (Supplementary Table 2). The panel was finalized after 58 optimization runs, supported by the Lunaphore COMET priority access platform for evaluating intensity, sensitivity, elution efficacy, incubation time, antibody dilution, exposure time and cycle position. For the SeqIF stainings, samples were sectioned on a cryotome (8 µm) and collected on adhesion slides (Epredia SuperFrost Ultra Plus GOLD; Thermo Fisher Scientific) and dried on a 37 °C heat plate for 15 minutes. After storage at −80 °C, sections were brought to room temperature and were incubated in 4% formaldehyde for 40 minutes at room temperature. Samples were washed for 5 minutes at room temperature in Multistaining Buffer (Lunaphore Technologies, BU06), followed by incubation with Multistaining Buffer supplemented with 0.2% Triton for 20 minutes at room temperature. Subsequently, slides were stored in Multistaining Buffer until use. Slides were dried off and placed into COMET stainers with microfluidic chips positioned on top of the tissue section as described by Rivest et al.[48]. Antibody mixes were prepared by diluting the stock antibody solutions in Intercept-T20 to help with blocking of non-specific binding (Supplementary Table 2). Automated SeqIF staining and imaging were performed on the COMET platform (Lunaphore Technologies). Slides underwent 13 cycles of iterative staining and imaging, followed by elution of the primary and secondary antibodies[75]. The 16-plex protocol template was generated using COMET Control Software, and reagents were loaded onto the device to perform the SeqIF protocol. A list of primary antibodies with corresponding incubation times can be found in Supplementary Table 2. Secondary antibodies were used as a mix of two species-complementary antibodies: Alexa Fluor Plus 647 goat anti-rabbit (Thermo Fisher Scientific, cat no. A32733, 1:250 dilution) and Alexa Fluor Plus 555 goat anti-rat (Thermo Fisher Scientific, cat no. A48263, 1:250 dilution). Nuclear signal was detected using DAPI (Thermo Fisher Scientific, cat no. D1306, 1:1,000 dilution) by dynamic incubation of 2 minutes. All reagents, if not otherwise stated, were diluted in Multistaining Buffer (Lunaphore Technologies, BU06). The elution step lasted 2 minutes for each cycle and was performed with Elution Buffer (Lunaphore Technologies, BU07-L) at 37 °C. The quenching step lasted for 30 seconds and was performed with Quenching Buffer (Lunaphore Technologies, BU08-L). The imaging step was performed with Imaging Buffer (Lunaphore Technologies, BU09). The output from the COMET platform is a stitched and registered, multistack OME-TIFF file that was directly used for further processing with MCMICRO and downstream applications[49].

Image processing and analysis of SeqIF (Lunaphore COMET data)

Post-acquisition registration of full-slide images was needed for two images due to interrupted runs and was performed with Palom (https://github.com/labsyspharm/palom). Processing of multichannel OME-TIFF files was performed using a modified version of MCMICRO[49]. Raw marker intensities were corrected for autofluorescence signal with Backsub (https://github.com/schapirolabor/background_subtraction)

by subtracting the respective autofluorescence image intensity scaled to each marker's exposure time. The corrected intensity was computed using equation (1): $\text{Marker}_{\text{corrected}} = \text{Marker}_{\text{raw}} - \text{Background} \times \text{Exposure}_{\text{Marker}} / \text{Exposure}_{\text{Background}}$. Preprocessing of the images to improve segmentation was performed using CLAHE on the DAPI and membrane (WGA) channels. Cell segmentation was performed similarly to Molecular Cartography data using CLAHE-adjusted images to train a custom Cellpose 2 model via the human-in-the-loop approach. Feature quantification was performed on the autofluorescence-subtracted images based on the labeled segmentation masks. To assign cell phenotypes, we used a pixel-level clustering workflow using SOMs implemented via the Pixie pipeline[50]. For that purpose, we manually annotated the image region containing the heart using QuPath (0.4.3, MacOS version) and set all background pixels to 0 across all channels to reduce the number of pixels to be processed by Pixie[72]. We then performed pixel clustering with 10 functional markers: Ankrd1, αSMA, CCR2, CD31, CD45, CD68, Mpo, Pdgfra, Tnnt2 and Trem2 across all nine COMET images using 5% of pixel subsets to train the SOM. Pixel meta-clusters were visualized using the Pixie Jupyter widget, and 100 SOM clusters were manually merged and visualized as pixel phenotype maps for validation. Pixel clusters were subsequently used in a second clustering step with Cellpose masks to assign cell phenotypes via SOM clustering across all images. Similar to pixel clustering, 100 SOM clusters were manually merged into cell phenotypes, and each cell segmentation mask was assigned a phenotype. For phenotyping accuracy evaluation, we compared assigned cell phenotypes to an independently annotated subset of ground truth data and quantified performance using confusion matrices (raw and normalized) as well as per-class precision, recall and F1 scores (Supplementary Fig. 10). To quantify cell type abundances in different regions of the heart (endocardial infarct zone, epicardial infarct zone, infarct core and border zones), we manually annotated regions in QuPath and used them to subset cells based on their presence or absence in the annotation. For the quantification of myeloid cells in the endocardial infarct zone, we included cells in the left ventricular lumen, only if they were in direct contact with endocardial cells. Endothelial cells in the manually annotated endocardial layer were assigned as 'Endocardial cells'. The endocardial infarct zone was annotated as the endocardial layer and the adjacent 2–3-cell-thick layer of cardiomyocytes expressing Tnnt2 near the infarct core, not including papillary muscles. The infarct core was defined based on heart geometry in the region where the infarct was transmural. The epicardial infarct zone was annotated as the epicardial layer and a 3–4-cell-thick layer along the infarct core. The border zone was annotated as the border region of the infarct including both stressed and Tnnt2-expressing cardiomyocytes. The remote endocardial region was annotated as the endocardial layer and a 3–4-cell-thick region on the opposite side of the lumen to the infarct core with no nearby stressed cardiomyocytes, and the same applies for the control samples. The areas outside the tissue samples are denoted as 'Background', and the areas within the left ventricular lumen were annotated as 'Lumen'. Matching the size thresholds adapted for pixel size from Molecular Cartography data, cells with an area below 72 and above 72,000 pixels were excluded. Additionally, cells were filtered based on small size, low solidity and high eccentricity. Based on the distance of each cell to the lumen, cells were binned into strips with 18.4-µm thickness (Extended Data Fig. 6). A Minerva Story was created using Minerva Author for a representative sample 24 hours after MI[76,77].

Segmentation method comparison

To create an evaluation of used segmentation models DeepCell Mesmer 'nuclear' and 'whole-cell', Cellpose 'cyto' and our custom-trained Cellpose 2 model, we selected an additional 16 crops (500 × 500 pixels) spanning four representative regions per timepoint and independently annotated the ground truth cells based on the CLAHE-adjusted nuclear and membrane markers using the napari toolkit[33,34,42,63]. The crops included a total of 1,208 ground truth annotations ranging from 37 to 112 cells per crop, with total counts of cells per timepoint ranging from 253 to 357.

Segmentation evaluation was performed on a crop-level basis using an object-based approach as described in Greenwald et al.[33]. We constructed the cost matrix as 1 − Intersection over Union (IoU) for linear sum assignment. The cost matrix was padded to allow for unassigned cells with a penalty of 0.5. If an assigned ground truth and prediction pair had an IoU above 0.4, it was counted as a true-positive match. Ground truth cells without matches to prediction cells were labeled false negatives, and prediction cells without matches to ground truth cells were labeled false positives. Unmatched ground truth and prediction cells were used as nodes in a graph with edges between them if they had an IoU above 0.1 to account for tissue density. According to Greenwald et al., merges are defined as events where multiple ground truth cells are connected to one prediction cell; splits are defined as events where one ground truth cell is connected to multiple prediction cells; and catastrophes are defined as events where multiple ground truth cells are connected to multiple prediction cells. An example image (crop of sample_d1.r1 of the SeqIF dataset) is provided to highlight observed segmentation errors (Extended Data Fig. 2a).

Across the annotated 1,208 ground truth cells, DeepCell Mesmer 'nuclear' had 353 true positives, 400 false positives, 855 false negatives, 12 merges, nine splits and two catastrophes. DeepCell Mesmer 'whole-cell' had 567 true positives, 515 false positives, 641 false negatives, 49 merges, 31 splits and 38 catastrophes. Cellpose 'cyto' had 521 true positives, 194 false positives, 687 false negatives, 28 merges, three splits and five catastrophes, and our custom Cellpose model had 1,124 true positives, 124 false positives, 84 false negatives, four merges, six splits and two catastrophes (Supplementary Fig. 3b). IoU and Dice scores were measured for each true-positive pair, and the mean value was calculated per image crop. Precision, recall and F1 score were also calculated on a per-crop basis and highlighted our custom model outperforming the other methods on this specific dataset (Extended Data Fig. 2c).

Additionally, we provide the segmented percentage of the tissue in SeqIF data calculated as the percentage of recovered tissue not within 'Background' or 'Lumen' annotations. We also provide the percentage of assigned transcripts in the Molecular Cartography data. Both metrics highlight that our custom model recovers the most relevant tissue information (Extended Data Fig. 2d). Taken together, using our custom Cellpose models (for SeqIF and Molecular Cartography), we were able to recover more tissue area than we could with existing models without sacrificing accuracy on this specific dataset.

Laser microdissection coupled to ultrasensitive proteomics

To collect cells with a Leica Laser Microdissection 7 (LMD7) microscope, three reference points are required to triangulate the shape coordinates into laser cutting coordinates. These reference points were etched using the LMD7 on the membrane of the Leica Frame slides (order no. 11600294) before the tissues were placed on them. These etchings were easily recognizable features to which we could go back and designate them as reference points. Five-micrometer-thick tissue sections from fresh-frozen heart tissue were prepared similarly to the SeqIF samples and were placed onto Leica Frame slides with reference points. Slides were stained using DAPI, WGA and CD31 (as described in the immunofluorescence subsection) and imaged using a Zeiss Axioscan 7. Stitched images of whole hearts were imported and annotated in QuPath for downstream laser capture microdissection. Endocardial regions to be collected by the LMD7 were annotated using QuPath's brush tool with a brush diameter of approximately 20 µm, centered around endocardial cells with 10 µm to each side as buffer for the laser cutting. For control hearts, only one endocardial group was annotated, whereas, for hearts, 1-day post-infarct endocardial cells in the infarct region and endocardial cells in the remote region were labeled separately. QuPath annotations were then exported as GeoJSON files, which were further processed using the Qupath_to_LMD scripts

(https://github.com/CosciaLab/Qupath_to_LMD). The script assigns annotation classes to wells of the 384-well plate. It uses the py-lmd package from Madler et al. (https://github.com/MannLabs/py-lmd) to transfer GeoJSON polygons into LMD readable .xml files.

Laser capture microdissection

We used the Leica LMD7 system and Leica Laser Microdissection version 8.3.0.08259 software to collect tissue contours. Tissue was cut with a ×63 objective (HC PL FLUOTAR L ×63/0.70 CORR XT) in brightfield mode. Laser settings were as follows: power 60; aperture 1; speed 25; middle pulse count 2; final pulse 5; head current 39–41%; pulse frequency 2,028; and offset 105. Contours were cut and sorted into a low-binding 384-well plate (Eppendorf, 0030129547) configured over the 'universal holder' function.

Sample preparation for liquid chromatography–mass spectrometry analysis

To collect tissue pieces stuck on the sides of the 384 wells, we washed them down with 30 µl of acetonitrile, briefly vortexed and vacuum dried (15 minutes at 60 °C). We added 2 µl of Lysis Buffer (0.1% DDM, 5 mM TCEP, 20 mM CAA resuspended in 100 mM TEAB (pH 8.5)) to each well, closed the plate with a PCR ComfortLid (Hamilton) and heated at 95 °C for 60 minutes. We added 1 µl of LysC (2 ng µl^{-1} in water) and incubated for at least 2 hours at 37 °C. Subsequently, 1 µl of trypsin was added (1 ng µl^{-1} in water), and the samples were incubated overnight at 37 °C. The next day, the samples were vacuum dried before peptide cleanup. Peptide cleanup took place with Evotips (Evosep) following the manufacturer's recommendations. In brief, the Evotips (EV2013, Evotip Pure) were washed with Buffer B (99.9% acetonitrile, 0.1% formic acid) and then Buffer A (99.9% water, 0.1% formic acid) and then activated with isopropanol. Digested tissue samples were resuspended in Buffer A, loaded into the tips, washed with Buffer A once and then eluted with Buffer B into a 96-well plate (Thermo Fisher Scientific, AB1300) and vacuum dried. Samples were stored at −20 °C until liquid chromatography–mass spectrometry (LC–MS) analysis. For LC–MS analysis, 4.2 µl of MS loading buffer (3% acetonitrile, 0.1% trifluoroacetic acid in water) was added, from which 4.0 µl was finally injected into the mass spectrometer.

LC–MS analysis

LC–MS analysis was performed with an EASYnLC-1200 system (Thermo Fisher Scientific) connected to a trapped ion mobility spectrometry quadruple time-of-flight mass spectrometer (timsTOF SCP; Bruker Daltonik) with a nano-electrospray ion source (CaptiveSpray; Bruker Daltonik). Peptides were loaded on a 20-cm home-packed high-performance liquid chromatography column (75-µm inner diameter packed with 1.9-µm ReproSil-Pur C18-AQ silica beads; Dr. Maisch). Peptides were separated using a linear gradient of 21 minutes and analyzed in dia-PASEF mode.

Proteomics data analysis

We used DIA-NN (1.8.2) for dia-PASEF raw file analysis, and the generated libraries were used for mouse proteins (UniProt mouse released in 2021) and known contaminants[78]. Deep-learning-based spectra, retention times and ion mobility predictions were enabled for the appropriate mass range of 300–1,200 m/z. N-terminal M excision and cysteine carbamidomethylation were enabled as fixed modifications. A maximum of two miscleavages were allowed, and the precursor charge was set to 2–4. DIA-NN was operated in the default mode with minor adjustments. In brief, MS1 and MS2 accuracies were set to 15.0; scan windows were set to 0 (assignment by DIA-NN); and isotopologues were enabled, as were matched-between-runs, heuristic protein inference and no shared spectra. Proteins were inferred from genes; neural network classifiers were set to single-pass mode; and quantification strategy was set as 'Robust LC (high precision)'. Cross-run normalization was set to 'RT-dependent', library generation as 'smart profiling' and speed and RAM usage as 'optimal results'. Protein lists were filtered for missing values by group, requiring at least two observed values in the control group or three observed values in the MI remote or MI IZ group. We also filtered out known contaminants based on previously described contaminants libraries[78]. Differential protein expression analysis was performed on data normalized using variance stabilizing normalization using empirical Bayes statistics in limma[79]. Proteins with a false discovery rate lower than 0.05 were considered as significantly differentially expressed. Overlap in the proteins differentially expressed between conditions was visualized using UpSet plots with the ComplexUpset package[80]. Endocardial specificity of DEPs was compared by correlating log fold changes from DEP analysis with log fold changes from marker gene estimations (Seurat's FindMarkers function) for endocardial cells from sham controls from the reprocessed Calcagno et al. [22] dataset (see the 'Single-cell analysis of Molecular Cartography data' subsection).

Analysis of human CITE–seq data

Processed CITE–seq data from Amrute et al.[52] were received from the original authors as a processed Seurat object (version 4.0.0)[52]. Cell type annotations from the original authors were used to visualize cell types on the UMAP plot. Differential expression of vWF between donor and acute MI samples was performed by calculating pseudobulk expression per sample and performing DESeq analysis between pseudobulk expression of donor ($n = 6$) and acute MI ($n = 4$) samples. Normalized RNA expression was visualized per group using violin plots from the SCpubr package[81].

Echocardiography

Echocardiographic analyses were performed in conscious mice using a Vevo 2100 ultrasound system (VisualSonics). Left ventricular end-diastolic volume, end-systolic volume and ejection fraction were measured based on the left parasternal long-axis view and were acquired using VevoLab software (VisualSonics). Global longitudinal strain was quantified in the longitudinal axis by speckle tracking using VevoStrain software (VisualSonics). Investigators were blinded to the sample group allocation during the experiments and analyses.

Flow cytometry

Single-cell suspensions of infarcted hearts were obtained by mincing the tissue with fine scissors and digesting it with a solution containing 450 U ml^{-1} Collagenase I, 125 U ml^{-1} Collagenase XI, 60 U ml^{-1} DNase I and 60 U ml^{-1} hyaluronidase (MilliporeSigma) for 1 hour at 37 °C while shaking. For flow cytometry of blood samples, erythrocytes were lysed in red blood cell lysis buffer (Miltenyi Biotec). The fluorescent antibodies are described in Supplementary Table 3. Flow cytometry was performed on a FACSVerse (BD Biosciences). Data were analyzed using FlowJo software. Mo/Mϕ were identified as CD45$^+$, Lin$^-$(CD19;CD4;NK1.1;Ly6G;Ter119) and CD11b$^+$.

Histology

Histopathological evaluation of left ventricular remodeling was performed on day 14 after MI induction. Hearts were excised and rinsed in PBS. After transverse sectioning using a scalpel, hearts were then embedded in OCT compound and placed in 2-methylbutane (Honeywell) on dry ice. Hearts were stored overnight at −80 °C and sectioned using a cryostat (9-µm thickness). Tissue sections were stained with a Masson's Trichrome Stain Kit (MilliporeSigma) according to the manufacturer's instructions. Scar thickness was averaged from five measurements in short axes in a blinded fashion.

Conventional immunofluorescence stainings

For conventional immunofluorescence staining, samples were sectioned on a cryotome (8 µm), collected on adhesion slides (Epredia SuperFrost Ultra Plus GOLD; Thermo Fisher Scientific) and dried on a

37 °C hot plate for 15 minutes. After storage at −80 °C, sections were brought to room temperature and incubated in 4% formaldehyde at room temperature for 40 minutes. Sections were permeabilized for 20 minutes, blocked with 5% BSA for 1 hour and stained overnight with primary antibodies for CD31, vWF, CCR2, CD68 or CD41 in 1% BSA staining buffer. On the following day, sections were washed and stained for 1 hour with the corresponding secondary antibodies combined with the labeled antibody against WGA. After washing, sections were stained with 300 nM DAPI (Thermo Fisher Scientific, D1306) for 10 minutes, washed again and covered with a mounting medium. For simultaneous staining of CCR2 and vWF, sections were fixed, permeabilized and blocked as described above. After incubating primary antibodies for CD31 and CCR2 overnight, vWF antibody was labeled using a secondary antibody labeling kit (FlexAble CoraLite Plus 750 Antibody Labeling Kit for Rabbit IgG; Proteintech). Labeling was carried out in accordance with the manufacturer's instructions. In brief, vWF primary antibody was incubated with FlexLinker and FlexBuffer for 5 minutes. FlexQuencher was added and incubated for five additional minutes. Then, 1% BSA staining buffer was added, and tissue sections were incubated with the labeled primary antibody. On the next day, sections were washed and stained with WGA conjugated to Alexa Fluor 488 (Thermo Fisher Scientific, W11261) for 1 hour. After the WGA incubation time, sections were stained with 300 nM DAPI (Thermo Fisher Scientific, D1306) for a duration of 10 minutes, washed again and covered with a mounting medium. Images were captured using an Axio Observer (Zeiss) fluorescence microscope and analyzed using QuPath (0.4.3, Windows version). In brief, cell segmentation was performed by using the cell detection tool based on DAPI staining. Mean cell intensity was used to define cells positive for Ccr2 (threshold 450) and Cd68 (threshold 400). An overview of antibodies used for conventional immunofluorescence stainings can be found in Supplementary Table 4.

Statistics and reproducibility

Mice were randomly assigned to different experimental groups. No exclusion of specific animals from the experiments was performed. All experiments were conducted on independent biological replicates: Molecular Cartography (two replicates per timepoint; technical replicates were only done to replace some initial samples that failed quality control and test correlation of measurements across slides/technical replicates); SeqIF (three controls; two replicates at 4 hours, 24 hours and 2 days after MI); and DVP (3–4 replicates per region). Human pseudobulk CITE–seq analyses included six healthy donors and four patients with acute MI from publicly available data. Functional blocking of vWF employed eight mice per experimental group. Sample size calculation was performed in G*Power 3.1 in accordance with the approved animal protocol and was based on our experience with similar experimental studies to achieve 80% power at a significance level of $P < 0.05$. Echocardiographic and histological analyses were performed in a blinded fashion.

Quantitative data are presented as mean ± s.d. Spatial distance measurements between cell types were compared by type II ANOVA on a linear OLS model, followed by two-sided post hoc *t*-tests with Bonferroni correction. Differential protein expression in endocardial regions was assessed with limma, employing variance stabilizing normalization and empirical Bayes statistics, with a false discovery rate of less than 0.05 defining significance. Human pseudobulk differential gene expression was determined by DESeq2. For functional measurements, comparisons between two groups were performed using unpaired two-tailed Student's *t*-test. Differences between more than two groups were analyzed by one-way ANOVA followed by Tukey's post hoc analysis or two-way ANOVA followed by Sidak's multiple comparison. Unless stated otherwise, $P < 0.05$ was considered statistically significant.

Reporting summary

Further information on research design is available in the Nature Portfolio Reporting Summary linked to this article.

Data availability

All relevant images and data for Molecular Cartography and SeqIF described in this study are publicly available via Synapse (project SynID: syn51449054): https://www.synapse.org/Synapse:syn51449054. The mass spectrometry proteomics data have been deposited to the ProteomeXchange Consortium via the PRIDE partner repository with the dataset identifier PXD066993.

A Minerva Story with a detailed and interactive exploration of a 24-hour post-MI sample is available at https://schapirolabor.github.io/mi_spatialomics_minerva_story_d1.

Code availability

All code to process data and produce the results presented in this paper is available on Github: https://github.com/SchapiroLabor/mi_spatialomics.

References

1. Yan, X. et al. Temporal dynamics of cardiac immune cell accumulation following acute myocardial infarction. *J. Mol. Cell. Cardiol.* **62**, 24–35 (2013).
2. Khan, M. A. B. et al. Global epidemiology of ischemic heart disease: results from the Global Burden of Disease study. *Cureus* **12**, 9349 (2020).
3. Laforgia, P. L., Auguadro, C., Bronzato, S. & Durante, A. The reduction of mortality in acute myocardial infarction: from bed rest to future directions. *Int. J. Prev. Med.* **13**, 56 (2022).
4. Asaria, P. et al. Acute myocardial infarction hospital admissions and deaths in England: a national follow-back and follow-forward record-linkage study. *Lancet Public Health.* **2**, e191–e201 (2017).
5. Kochar, A. et al. Long-term mortality of older patients with acute myocardial infarction treated in US clinical practice. *J. Am. Heart Assoc.* **7**, e007230 (2018).
6. Tsao, C. W. et al. Heart disease and stroke statistics—2022 update: a report from the American Heart Association. *Circulation* **145**, e153–e639 (2022).
7. Kologrivova, I., Shtatolkina, M., Suslova, T. & Ryabov, V. Cells of the immune system in cardiac remodeling: main players in resolution of inflammation and repair after myocardial infarction. *Front. Immunol.* **12**, 664457 (2021).
8. Liu, J., Wang, H. & Li, J. Inflammation and inflammatory cells in myocardial infarction and reperfusion injury: a double-edged sword. *Clin. Med. Insights Cardiol.* **10**, CMC.S33164 (2016).
9. Nagai, T. et al. Decreased myocardial dendritic cells is associated with impaired reparative fibrosis and development of cardiac rupture after myocardial infarction in humans. *J. Am. Heart Assoc.* **3**, e000839 (2014).
10. Ong, S.-B. et al. Inflammation following acute myocardial infarction: multiple players, dynamic roles, and novel therapeutic opportunities. *Pharmacol. Ther.* **186**, 73–87 (2018).
11. Nian, W., Huang, Z. & Fu, C. Immune cells drive new immunomodulatory therapies for myocardial infarction: from basic to clinical translation. *Front. Immunol.* **14**, 1097295 (2023).
12. Rusinkevich, V. et al. Temporal dynamics of immune response following prolonged myocardial ischemia/reperfusion with and without cyclosporine A. *Acta Pharmacol. Sin.* **40**, 1168–1183 (2019).
13. Boufenzer, A. et al. TREM-1 mediates inflammatory injury and cardiac remodeling following myocardial infarction. *Circ. Res.* **116**, 1772–1782 (2015).
14. Cochain, C. et al. The chemokine decoy receptor D6 prevents excessive inflammation and adverse ventricular remodeling after myocardial infarction. *Arter. Thromb. Vasc. Biol.* **32**, 2206–2213 (2012).
15. Zouggari, Y. et al. B lymphocytes trigger monocyte mobilization and impair heart function after acute myocardial infarction. *Nat. Med.* **19**, 1273–1280 (2013).

16. Krishnamurthy, P. et al. IL-10 inhibits inflammation and attenuates left ventricular remodeling after myocardial infarction via activation of STAT3 and suppression of HuR. *Circ. Res.* **104**, e9–e18 (2009).
17. Nahrendorf, M. et al. The healing myocardium sequentially mobilizes two monocyte subsets with divergent and complementary functions. *J. Exp. Med.* **204**, 3037–3047 (2007).
18. Jin, K. et al. Single-cell RNA sequencing reveals the temporal diversity and dynamics of cardiac immunity after myocardial infarction. *Small Methods* **6**, 2100752 (2022).
19. Rizzo, G. et al. Dynamics of monocyte-derived macrophage diversity in experimental myocardial infarction. *Cardiovasc. Res.* **119**, 772–785 (2023).
20. Zhuang, L. et al. Global characteristics and dynamics of single immune cells after myocardial infarction. *J. Am. Heart Assoc.* **11**, e027228 (2022).
21. Papalexi, E. & Satija, R. Single-cell RNA sequencing to explore immune cell heterogeneity. *Nat. Rev. Immunol.* **18**, 35–45 (2018).
22. Calcagno, D. M. et al. Single-cell and spatial transcriptomics of the infarcted heart define the dynamic onset of the border zone in response to mechanical destabilization. *Nat. Cardiovasc. Res.* **1**, 1039–1055 (2022).
23. Yamada, S. et al. Spatiotemporal transcriptome analysis reveals critical roles for mechano-sensing genes at the border zone in remodeling after myocardial infarction. *Nat. Cardiovasc. Res.* **1**, 1072–1083 (2022).
24. Kuppe, C. et al. Spatial multi-omic map of human myocardial infarction. *Nature* **608**, 766–777 (2022).
25. Bressan, D., Battistoni, G. & Hannon, G. J. The dawn of spatial omics. *Science* **381**, eabq4964 (2023).
26. Lewis, S. M. et al. Spatial omics and multiplexed imaging to explore cancer biology. *Nat. Methods* **18**, 997–1012 (2021).
27. Kiessling, P. & Kuppe, C. Spatial multi-omics: novel tools to study the complexity of cardiovascular diseases. *Genome Med.* **16**, 14 (2024).
28. Moses, L. & Pachter, L. Museum of spatial transcriptomics. *Nat. Methods* **19**, 534–546 (2022).
29. Park, J. et al. Spatial omics technologies at multimodal and single cell/subcellular level. *Genome Biol.* **23**, 256 (2022).
30. Zeng, H. et al. Spatially resolved single-cell translatomics at molecular resolution. *Science* **380**, eadd3067 (2023).
31. Amitay, Y. et al. CellSighter: a neural network to classify cells in highly multiplexed images. *Nat. Commun.* **14**, 4302 (2023).
32. Edlund, C. et al. LIVECell—a large-scale dataset for label-free live cell segmentation. *Nat. Methods* **18**, 1038–1045 (2021).
33. Greenwald, N. F. et al. Whole-cell segmentation of tissue images with human-level performance using large-scale data annotation and deep learning. *Nat. Biotechnol.* **40**, 555–565 (2022).
34. Pachitariu, M. & Stringer, C. Cellpose 2.0: how to train your own model. *Nat. Methods* **19**, 1634–1641 (2022).
35. Sicklinger, F. et al. A minimal-invasive approach for standardized induction of myocardial infarction in mice. *Circ. Res.* **127**, 1214–1216 (2020).
36. Mund, A. et al. Deep Visual Proteomics defines single-cell identity and heterogeneity. *Nat. Biotechnol.* **40**, 1231–1240 (2022).
37. Galow, A.-M. et al. Integrative cluster analysis of whole hearts reveals proliferative cardiomyocytes in adult mice. *Cells.* **9**, 1144 (2020).
38. Skelly, D. A. et al. Single-cell transcriptional profiling reveals cellular diversity and intercommunication in the mouse heart. *Cell Rep.* **22**, 600–610 (2018).
39. Forte, E. et al. Dynamic interstitial cell response during myocardial infarction predicts resilience to rupture in genetically diverse mice. *Cell Rep.* **30**, 3149–3163 (2020).
40. Tombor, L. S. et al. Single cell sequencing reveals endothelial plasticity with transient mesenchymal activation after myocardial infarction. *Nat. Commun.* **12**, 681 (2021).
41. Farbehi, N. et al. Single-cell expression profiling reveals dynamic flux of cardiac stromal, vascular and immune cells in health and injury. *eLife* **8**, e43882 (2019).
42. Stringer, C., Wang, T., Michaelos, M. & Pachitariu, M. Cellpose: a generalist algorithm for cellular segmentation. *Nat. Methods* **18**, 100–106 (2021).
43. Tanevski, J., Flores, R. O. R., Gabor, A., Schapiro, D. & Saez-Rodriguez, J. Explainable multiview framework for dissecting spatial relationships from highly multiplexed data. *Genome Biol.* **23**, 97 (2022).
44. Dimitrov, D. et al. LIANA+ provides an all-in-one framework for cell–cell communication inference. *Nat. Cell Biol.* **26**, 1613–1622 (2024).
45. Houweling, A. C., van Borren, M. M., Moorman, A. F. & Christoffels, V. M. Expression and regulation of the atrial natriuretic factor encoding gene *Nppa* during development and disease. *Cardiovasc Res.* **67**, 583–593 (2005).
46. Tian, Y. et al. The spleen contributes importantly to myocardial infarct exacerbation during post-ischemic reperfusion in mice via signaling between cardiac HMGB1 and splenic RAGE. *Basic Res. Cardiol.* **111**, 62 (2016).
47. van Duijvenboden, K. et al. Conserved *NPPB*$^{+}$ border zone switches from MEF2- to AP-1–driven gene program. *Circulation* **140**, 864–879 (2019).
48. Rivest, F. et al. Fully automated sequential immunofluorescence (seqIF) for hyperplex spatial proteomics. *Sci. Rep.* **13**, 16994 (2023).
49. Schapiro, D. et al. MCMICRO: a scalable, modular image-processing pipeline for multiplexed tissue imaging. *Nat. Methods* **19**, 311–315 (2022).
50. Liu, C. C. et al. Robust phenotyping of highly multiplexed tissue imaging data using pixel-level clustering. *Nat. Commun.* **14**, 4618 (2023).
51. Gragnano, F. et al. The role of von Willebrand factor in vascular inflammation: from pathogenesis to targeted therapy. *Mediators Inflamm.* **2017**, 5620314 (2017).
52. Amrute, J. M. et al. Targeting immune–fibroblast cell communication in heart failure. *Nature* **635**, 423–433 (2024).
53. Petri, B. et al. von Willebrand factor promotes leukocyte extravasation. *Blood.* **116**, 4712–4719 (2010).
54. Braun, L. J. et al. Platelets docking to VWF prevent leaks during leukocyte extravasation by stimulating Tie-2. *Blood.* **136**, 627–639 (2020).
55. Gandhi, C., Motto, D. G., Jensen, M., Lentz, S. R. & Chauhan, A. K. ADAMTS13 deficiency exacerbates VWF-dependent acute myocardial ischemia/reperfusion injury in mice. *Blood.* **120**, 5224–5230 (2012).
56. Atiq, F. & O'Donnell, J. S. Novel functions for von Willebrand factor. *Blood.* **144**, 1247–1256 (2024).
57. Drakeford, C. et al. von Willebrand factor links primary hemostasis to innate immunity. *Nat. Commun.* **13**, 6320 (2022).
58. Sicklinger, F. et al. High-throughput echocardiography-guided induction of myocardial ischemia/reperfusion in mice. *Circ. Res.* **136**, 1099–1109 (2025).
59. Groiss, S. et al. Highly resolved spatial transcriptomics for detection of rare events in cells. Preprint at *bioRxiv* https://doi.org/10.1101/2021.10.11.463936 (2021).
60. Ewels, P. A. et al. The nf-core framework for community-curated bioinformatics pipelines. *Nat. Biotechnol.* **38**, 276–278 (2020).
61. Guerreiro, R., Wuennemann, F. & Todorov, P. ViriatoII/MindaGap: v0.0.3. *Zenodo* https://doi.org/10.5281/zenodo.8120559 (2023).

62. Pizer, S. M. et al. Adaptive histogram equalization and its variations. *Comput. Vis. Graph. Image Process.* **39**, 355–368 (1987).
63. Ahlers, J. et al. Napari: a multi-dimensional image viewer for Python. *Zenodo*. https://zenodo.org/records/8115575 (2023).
64. Hao, Y. et al. Integrated analysis of multimodal single-cell data. *Cell* **184**, 3573–3587 (2021).
65. Stuart, T. et al. Comprehensive integration of single-cell data. *Cell* **177**, 1888–1902 (2019).
66. Butler, A., Hoffman, P., Smibert, P., Papalexi, E. & Satija, R. Integrating single-cell transcriptomic data across different conditions, technologies, and species. *Nat. Biotechnol.* **36**, 411–420 (2018).
67. Satija, R., Farrell, J. A., Gennert, D., Schier, A. F. & Regev, A. Spatial reconstruction of single-cell gene expression data. *Nat. Biotechnol.* **33**, 495–502 (2015).
68. Hafemeister, C. & Satija, R. Normalization and variance stabilization of single-cell RNA-seq data using regularized negative binomial regression. *Genome Biol.* **20**, 296 (2019).
69. Hao, Y. et al. Dictionary learning for integrative, multimodal and scalable single-cell analysis. *Nat. Biotechnol.* **42**, 293–304 (2024).
70. Korsunsky, I. et al. Fast, sensitive and accurate integration of single-cell data with Harmony. *Nat. Methods* **16**, 1289–1296 (2019).
71. Kuhn, T. C. et al. Secretome analysis of cardiomyocytes identifies PCSK6 (proprotein convertase subtilisin/kexin type 6) as a novel player in cardiac remodeling after myocardial infarction. *Circulation* **141**, 1628–1644 (2020).
72. Bankhead, P. et al. QuPath: open source software for digital pathology image analysis. *Sci Rep.* **7**, 16878 (2017).
73. Virtanen, P. et al. SciPy 1.0: fundamental algorithms for scientific computing in Python. *Nat. Methods* **17**, 261–272 (2020).
74. Seabold, S. & Perktold, J. Statsmodels: econometric and statistical modeling with Python. in *Proc. Python in Sciences Conference* https://doi.org/10.25080/Majora-92bf1922-011 (SciPy, 2010).
75. Migliozzi, D. et al. Microfluidics-assisted multiplexed biomarker detection for in situ mapping of immune cells in tumor sections. *Microsyst. Nanoeng.* **5**, 59 (2019).
76. Hoffer, J. et al. Minerva: a light-weight, narrative image browser for multiplexed tissue images. *J. Open Source Softw.* **5**, 2579 (2020).
77. Rashid, R. et al. Narrative online guides for the interpretation of digital-pathology images and tissue-atlas data. *Nat. Biomed. Eng.* **6**, 515–526 (2022).
78. Frankenfield, A. M., Ni, J., Ahmed, M. & Hao, L. Protein contaminants matter: building universal protein contaminant libraries for DDA and DIA proteomics. *J. Proteome Res.* **21**, 2104–2113 (2022).
79. Ritchie, M. E. et al. limma powers differential expression analyses for RNA-sequencing and microarray studies. *Nucleic Acids Res.* **43**, e47 (2015).
80. Lex, A., Gehlenborg, N., Strobelt, H., Vuillemot, R. & Pfister, H. UpSet: visualization of intersecting sets. *IEEE Trans. Vis. Comput. Graph.* **20**, 1983–1992 (2014).
81. Blanco-Carmona, E. Generating publication ready visualizations for single cell transcriptomics using SCpubr. Preprint at *bioRxiv* https://doi.org/10.1101/2022.02.28.482303 (2022).

Acknowledgements

We gratefully acknowledge the data storage service SDS@hd, supported by the Ministry of Science, Research and the Arts Baden-Württemberg (MWK); support by the state of Baden-Württemberg through bwHPCl; and the German Research Foundation (DFG) through grants INST 35/1314-1 FUGG, INST 35/1503-1 FUGG and INST 35/1597-1 FUGG. F.W. was supported by a Walter Benjamin grant from the DFG (516668179) and the German Federal Ministry of Education and Research (BMBF, 01ZZ2004). J.N. and F.C. acknowledge support by the BMBF, as part of the National Research Initiatives for Mass Spectrometry in Systems Medicine, under grant agreement number 161L0222. D.S. is supported by the BMBF (01ZZ2004). F.L. acknowledges support from the DFG Collaborative Research Centre 1324 (subproject A07). F.S., C.H. and F.L. are supported by the DFG Collaborative Research Centre 1531 (subproject B07) and the DFG Graduate Research Training Group 2727. We thank W.-M. Vierdag (European Molecular Biology Laboratory) for help with napari, D. Dimitrov (European Molecular Biology Laboratory) for help with running LIANA+ and A. Dugourd (European Molecular Biology Laboratory) for help with differential protein expression analysis. F.S., J.M.A., K.J.L. and F.L. acknowledge support by the Leducq Foundation (ImmunoFib-HF). N.H. is supported by the MD/PhD program from the Faculty of Medicine at Heidelberg University. F.L. is thankful for support from the DFG Heisenberg Programme. D.S. and J.T. acknowledge support by the Bruno und Helene Jöster Stiftung and the Multi-dimensionAI project (CZS-Project number: P2022-08-101) was made possible by funding from the Carl-Zeiss-Stiftung. This work is also supported by the Health + Life Science Alliance Heidelberg Mannheim and received state funds approved by the State Parliament of Baden-Württemberg ('AI Health Innovation Cluster' and 'MULTI-SPACE'). For the publication fee, we acknowledge financial support by Heidelberg University. We thank our administrative and project management team: E. Schulz, L. Roeder, B. Haase and D. Sali.

Author contributions

F.W., F.S., F.L. and D.S. designed the study. F.S. performed mouse experiments and tissue embedding/sectioning. F.S., T.T. and N.H. performed conventional immunofluorescence stainings. F.S. and C.H. performed flow cytometry experiments. F.W., K.B., F.S. and M.A.I.-A. performed data analysis of Molecular Cartography data. J.T provided guidance for neighborhood analysis and performed MISTy analysis, under the supervision of J.S.-R. K.B., F.W., F.S., T.T. and M.C. performed SeqIF experiments and data analysis. J.N. performed ultrasensitive proteomics experiments. Interactive data visualization was created by K.B., with input from F.S., F.L., F.W. and D.S. Proteomics data analysis was done by J.N., F.W., F.S. and M.N., under the supervision of F.C. J.M.A. and K.J.L. provided and analyzed snRNA-seq data from human acute MI samples. F.S. performed functional blocking experiments for vWF. F.W., F.S., K.B., N.F., F.L. and D.S. wrote the paper, with input from all authors.

Competing interests

D.S. reports funding from GlaxoSmithKline and receiving fees/honoraria from ariadne.ai, GlaxoSmithKline, Immunai, Noetik, Alpenglow and Lunaphore. K.B. reports fees from Lunaphore. J.S.R. reports funding from GlaxoSmithKline, Pfizer and Sanofi and fees/honoraria from Travere Therapeutics, Stadapharm, Astex, Owkin, Pfizer and Grunenthal. F.W. is an employee of Seqera. The other authors declare no competing interests.

Additional information

Extended data is available for this paper at https://doi.org/10.1038/s44161-025-00717-y.

Supplementary information The online version contains supplementary material available at https://doi.org/10.1038/s44161-025-00717-y.

Correspondence and requests for materials should be addressed to Florian Leuschner or Denis Schapiro.

Peer review information *Nature Cardiovascular Research* thanks Clément Cochain, Charlotte Stadler and the other, anonymous, reviewer(s) for their contribution to the peer review of this work.

Reprints and permissions information is available at www.nature.com/reprints.

Publisher's note Springer Nature remains neutral with regard to jurisdictional claims in published maps and institutional affiliations.

Open Access This article is licensed under a Creative Commons Attribution-NonCommercial-NoDerivatives 4.0 International License, which permits any non-commercial use, sharing, distribution and reproduction in any medium or format, as long as you give appropriate credit to the original author(s) and the source, provide a link to the Creative Commons licence, and indicate if you modified the licensed material. You do not have permission under this licence to share adapted material derived from this article or parts of it. The images or other third party material in this article are included in the article's Creative Commons licence, unless indicated otherwise in a credit line to the material. If material is not included in the article's Creative Commons licence and your intended use is not permitted by statutory regulation or exceeds the permitted use, you will need to obtain permission directly from the copyright holder. To view a copy of this licence, visit http://creativecommons.org/licenses/by-nc-nd/4.0/.

© The Author(s) 2025

[1]Institute for Computational Biomedicine, Faculty of Medicine, University Hospital Heidelberg and Heidelberg University, Heidelberg, Germany. [2]Seqera, Barcelona, Spain. [3]Department of Internal Medicine III, University Hospital Heidelberg, Heidelberg, Germany. [4]German Centre for Cardiovascular Research (DZHK), partner site Heidelberg, Heidelberg, Germany. [5]Max Delbrück Center for Molecular Medicine in the Helmholtz Association (MDC), Spatial Proteomics Group, Berlin, Germany. [6]Charité – Universitätsmedizin Berlin, corporate member of Freie Universität Berlin and Humboldt Universität zu Berlin, Berlin, Germany. [7]Center for Cardiovascular Research, Department of Medicine, Cardiovascular Division, Washington University School of Medicine, St. Louis, MO, USA. [8]Translational Spatial Profiling Center (TSPC), Heidelberg, Germany. [9]European Molecular Biology Laboratory, European Bioinformatics Institute (EMBL-EBI), Hinxton, UK. [10]Institute of Pathology, University Hospital Heidelberg, Heidelberg, Germany. [11]These authors contributed equally: Florian Wünnemann, Florian Sicklinger, Florian Leuschner, Denis Schapiro. ✉e-mail: florian.leuschner@med.uni-heidelberg.de; denis.schapiro@uni-heidelberg.de

https://doi.org/10.1038/s44161-025-00717-y

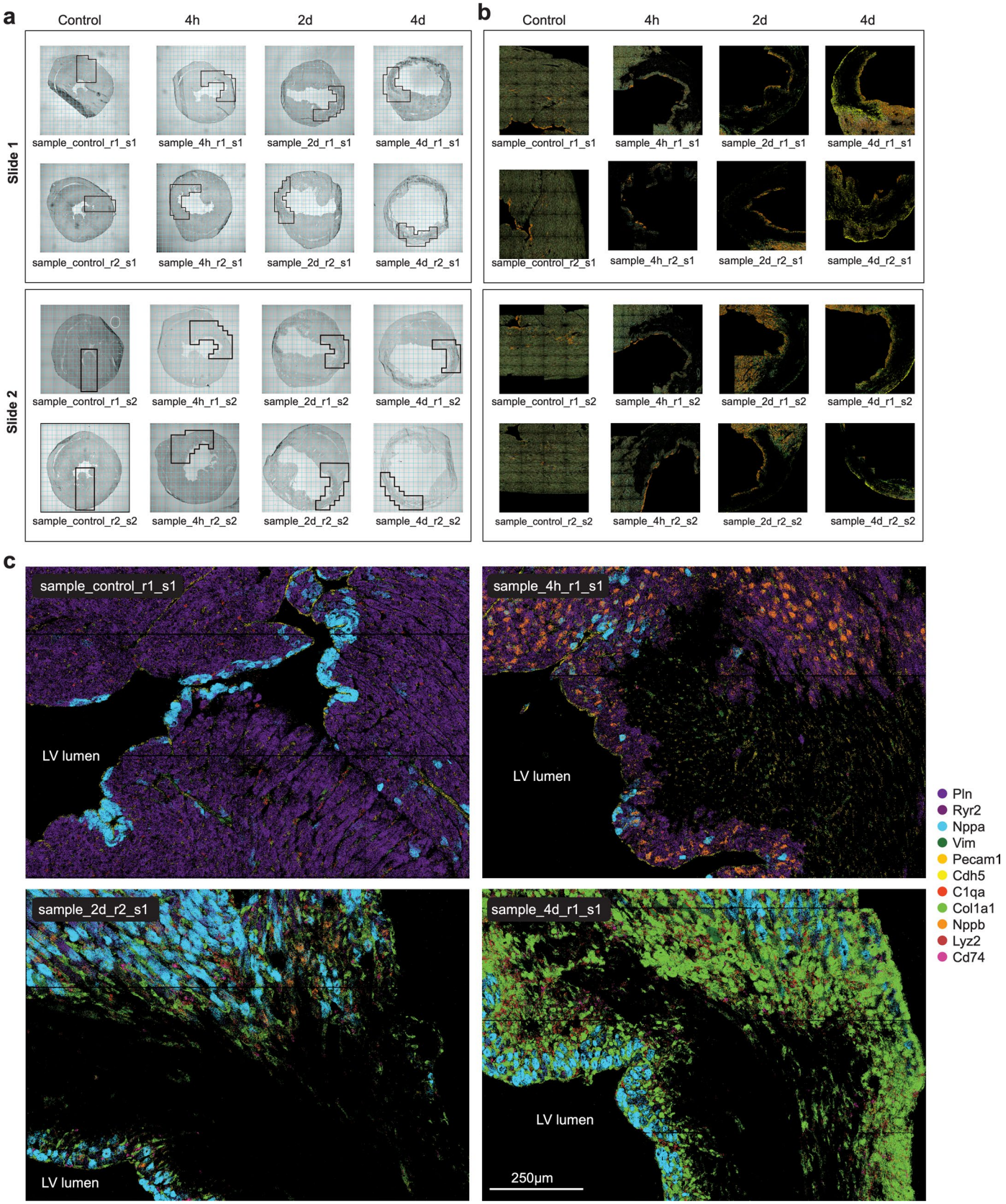

Extended Data Fig. 1 | Region of interest (ROI) selection and spot distribution of mouse heart sections from Molecular Cartography. a) Brightfield images of transverse sections of mouse hearts at different time points during acute MI (Control = prior to infarct). Black rectangles highlight regions selected for Molecular Cartography. **b**) Molecular Cartography RNA spots (100-plex) for corresponding regions highlighted in **a**). Regions with low spot density within the tissue at the 4 h, 2 d and 4 d post-MI timepoints demarcate infarct regions with cell death, apoptosis and RNA degradation. Note that images in **b**) show scatterplots of RNA spot centroid positions after spot calling by Resolve Bioscience and not the raw FISH signals. **c**) Exemplar regions of RNA expression maps of indicated markers over all 4 timepoints.

https://doi.org/10.1038/s44161-025-00717-y

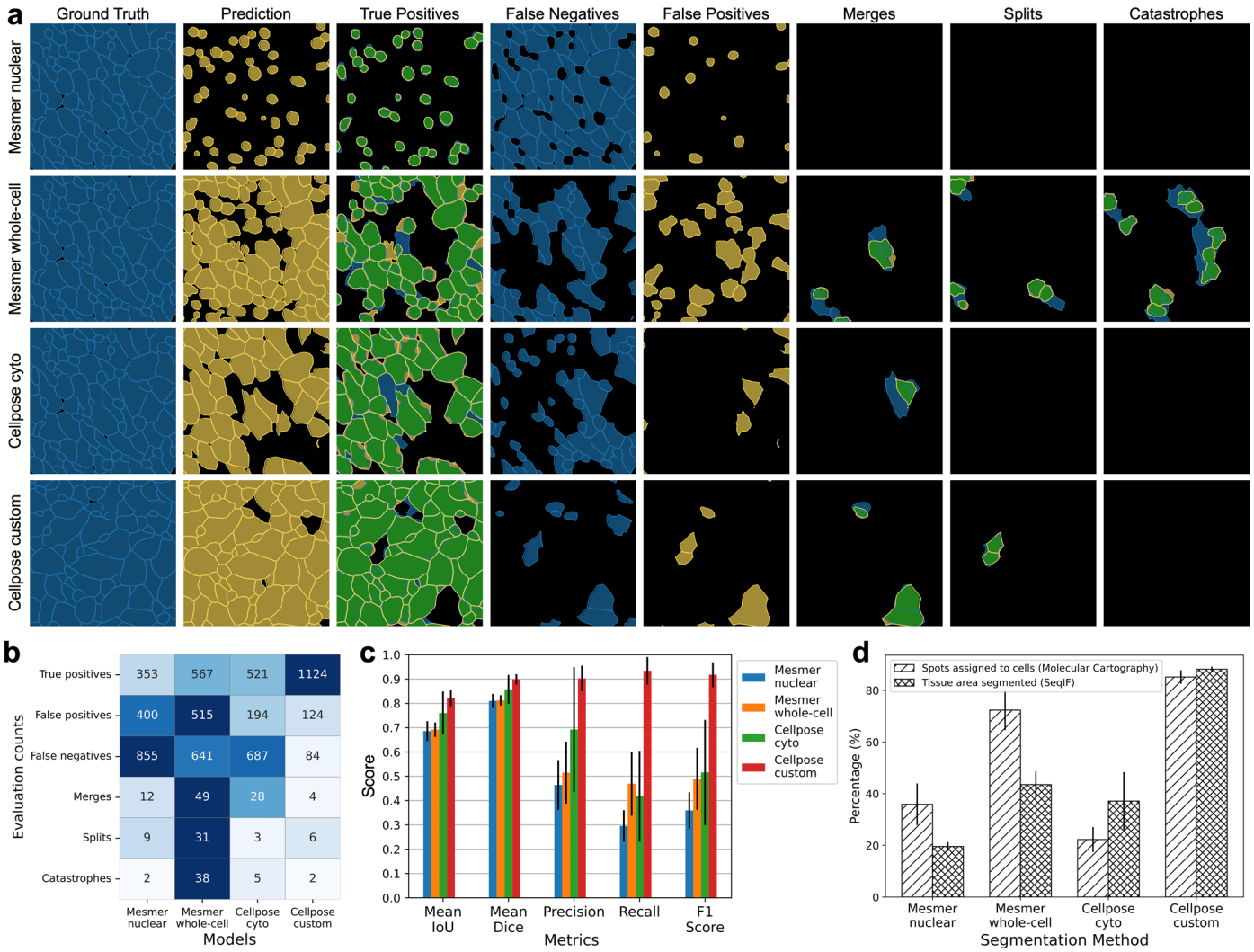

Extended Data Fig. 2 | Comparison of segmentation methods for Molecular Cartography and SeqIF heart sections. a) Example evaluation on a single image of 4 segmentation models across 8 panels: ground truth (blue) and prediction (yellow) panels show all ground truth (GT) and predicted cells, respectively. True positives show GT regions in blue, prediction regions in yellow, and their overlaps in green. False negative panels show unmatched GT cells, and false positive panels show unmatched predicted cells. Merges, splits, and catastrophe panels show GT cells (blue), predictions (yellow), and their overlaps (green). **b**) Heatmap showing counts of true positives, false positives, false negatives, merges, splits, and catastrophes across the 4 segmentation models evaluated on independently annotated GT from 16 image crops (4 per time point) in the SeqIF dataset (total: 1208 cells). **c**) Segmentation evaluation metrics based on the GT annotations calculated on means of image-specific metrics, with error bars showing the standard deviation across images. **d**) Percentage of transcripts assigned to cells (Molecular Cartography) and percentage of segmented tissue area (SeqIF). Data show mean ± s.d.

https://doi.org/10.1038/s44161-025-00717-y

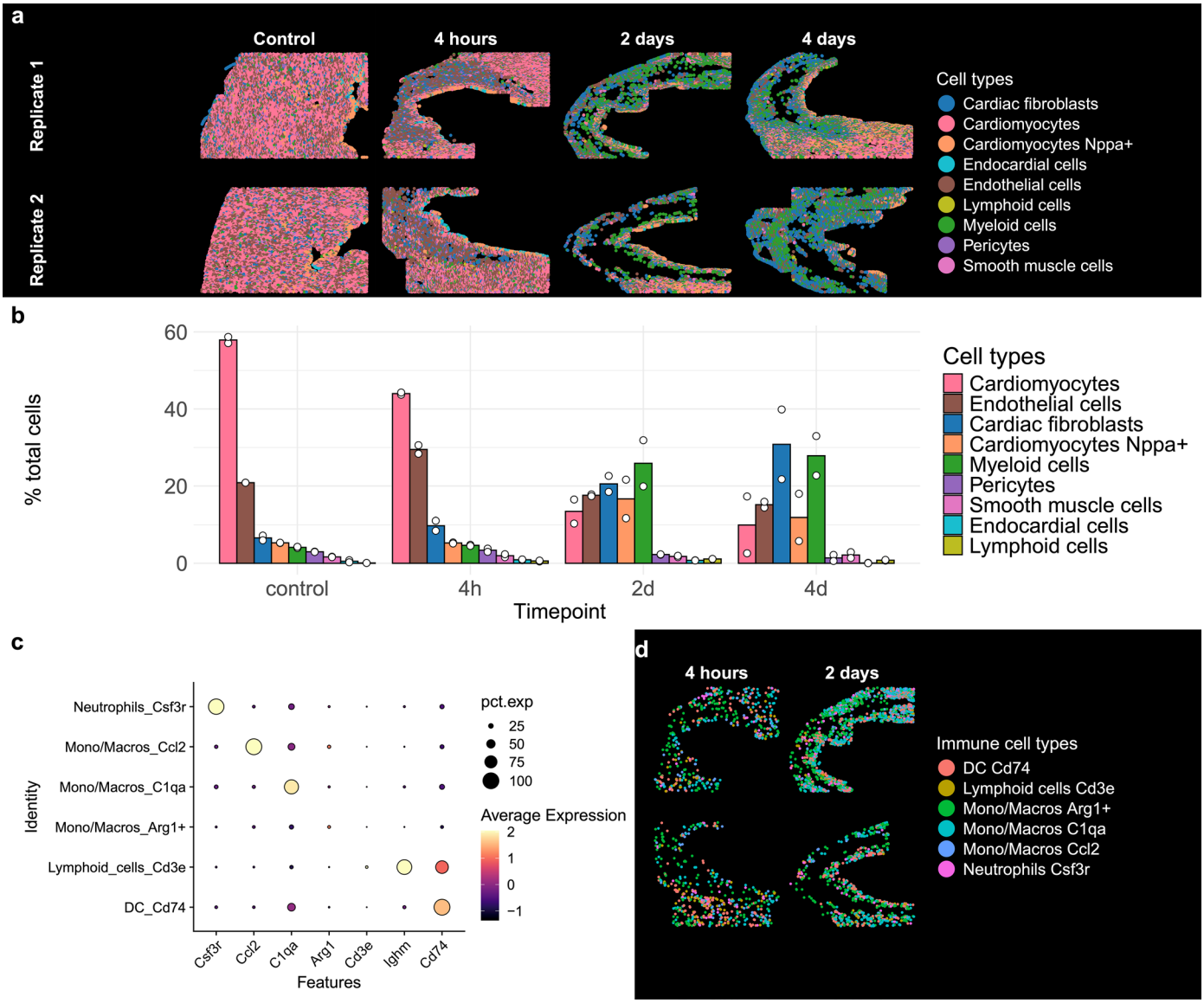

Extended Data Fig. 3 | Spatial cell type distribution and composition changes during acute MI as quantified by Molecular Cartography. a) Spatial distribution of cell-types in Molecular Cartography samples at four time points each with two biological replicates. **b**) Cell-type composition across acute myocardial infarction as quantified by Molecular Cartography. Barplots show mean percentage, points represent individual replicate measurements. **c**) Dotplot showing marker expression for identified immune cell subtypes. Immune subtype names are followed by their distinguishing marker with an underscore. **d**) Spatial distribution of these immune cell subtypes in two biological replicates for 4 h and 2 days.

https://doi.org/10.1038/s44161-025-00717-y

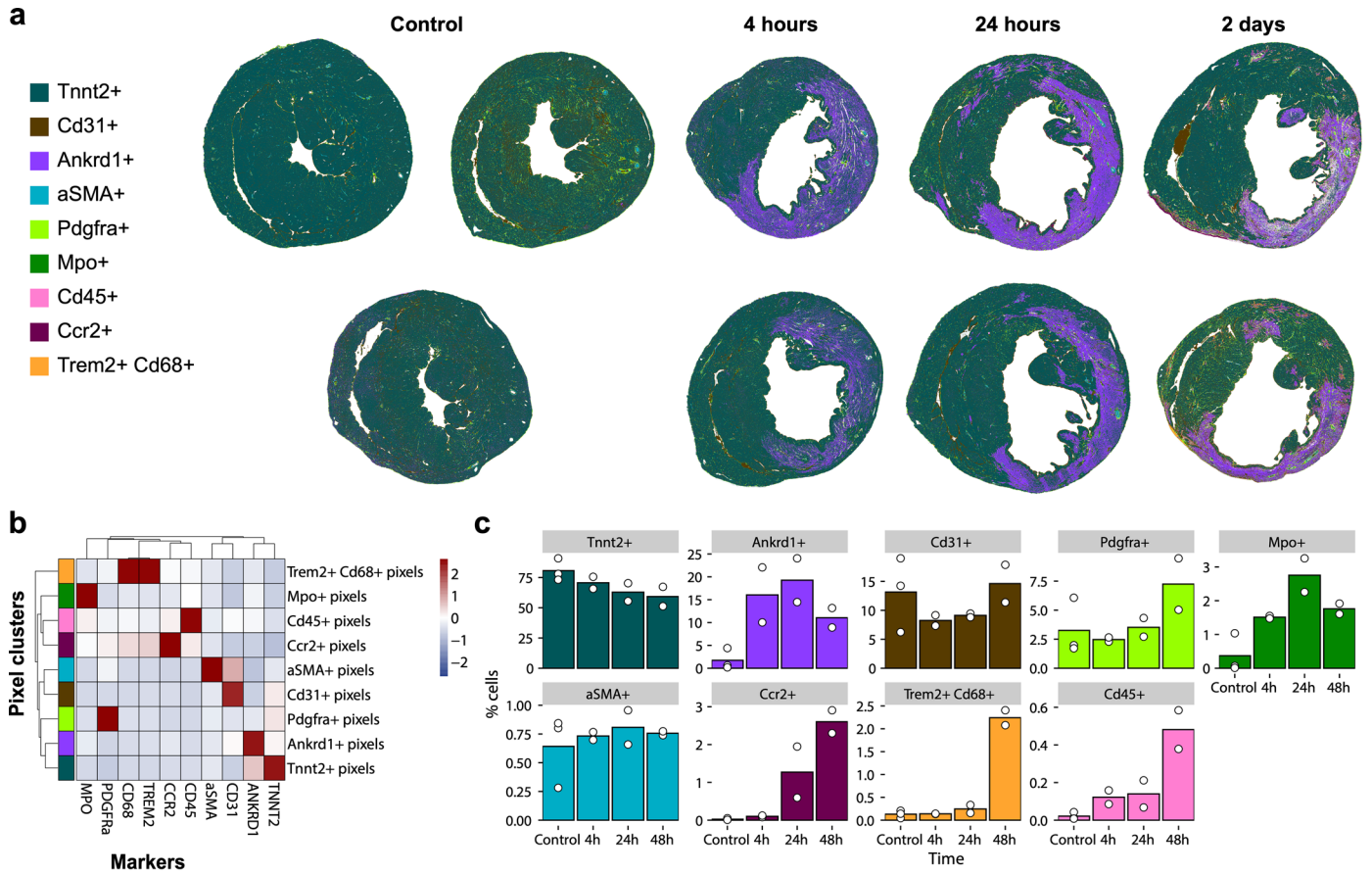

Extended Data Fig. 4 | SeqIF pixel clusters and cell phenotypes across acute MI time series. a) Pixel phenotype map for mouse heart images produced with SeqIF during a time course of acute myocardial infarction. Pixels were clustered using self-organizing maps leveraging Pixie and colored according to their assigned pixel cluster. A total of 9 different pixel clusters were classified. **b**) Heatmap of quantified marker expression in the corresponding pixel phenotype clusters. Colors for pixel clusters correspond to visualization in a. **c**) Quantification of pixel phenotypes across acute MI reveals strong reduction in Tnnt2+ pixels, increase in Ankrd1+ pixels and an increase in pixel clusters for myeloid cells (CD45+, Mpo+, Ccr2+, Trem2+, CD68+) during the first four days post MI. Colors correspond to pixel phenotypes visualization in a. Bars represent mean values from two biological replicates and points represent individual measurements. **d**) Zoom-ins for endocardial infarct zone regions from SeqIF images with corresponding cell typing highlighted. Top row shows SeqIF images with stainings for DNA (Hoechst = cyan), Cd31 (orange), Ccr2 (green) and Mpo (pink) at 3 different time points (4 h, 24 h and 48 h). Bottom row shows corresponding cell segmentations and cell types with endothelial cells (orange), Ccr2+ monocytes / macrophages (green) and neutrophils (pink). All other cell types are marked in grey for visualisation purposes.

https://doi.org/10.1038/s44161-025-00717-y

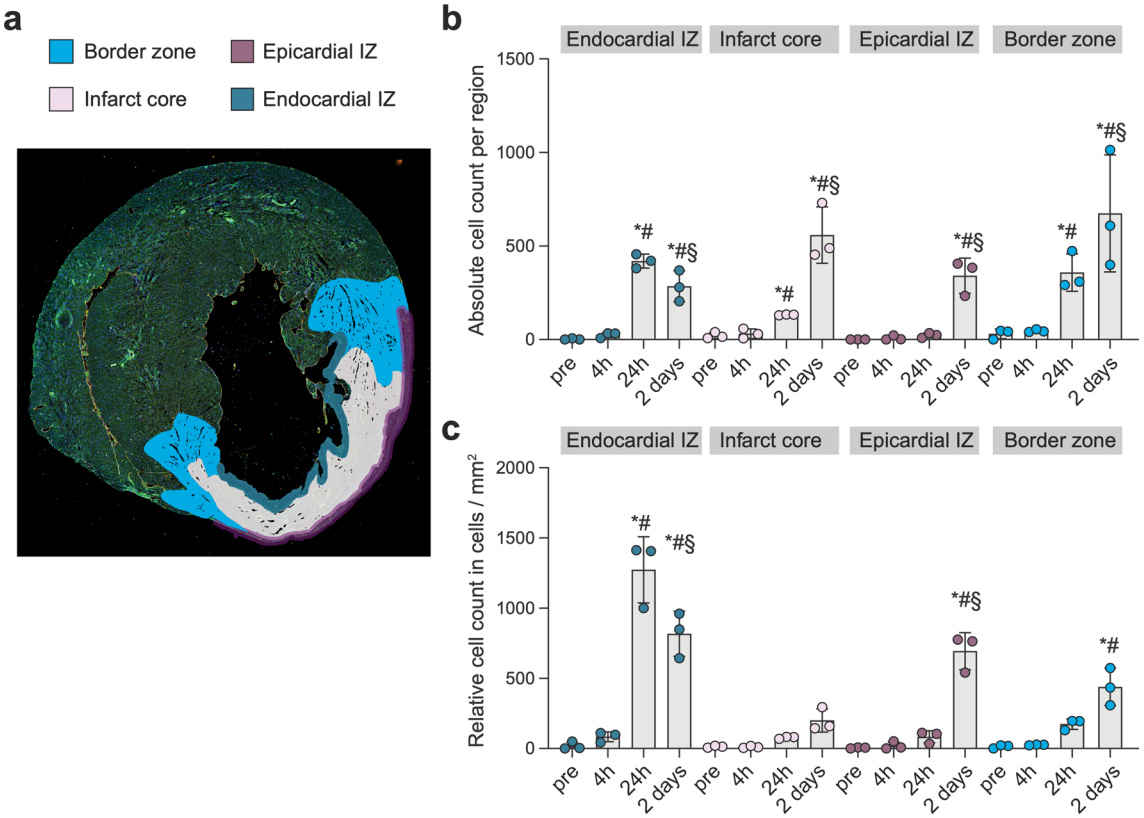

Extended Data Fig. 5 | Quantification of immune cell infiltration based on conventional IF imaging. a) Schematic highlighting different regions for quantification of immune cell infiltration. Absolute (**b**) and relative (**c**) numbers of CCR2 + /CD68+ Mo/Mϕ in different regions of the heart as depicted in a, using conventional immunofluorescence staining for CCR2, CD68, CD31, WGA and DAPI. Bars show mean abundance and points represent individual measurements. P values were determined by 2-way ANOVA followed by Tukey's multiple-comparison test. Only significant comparisons between timepoints within each region are displayed. *P < 0.05 vs. pre, #P < 0.05 vs. 4 h, §P < 0.05 vs. 24 h.

https://doi.org/10.1038/s44161-025-00717-y

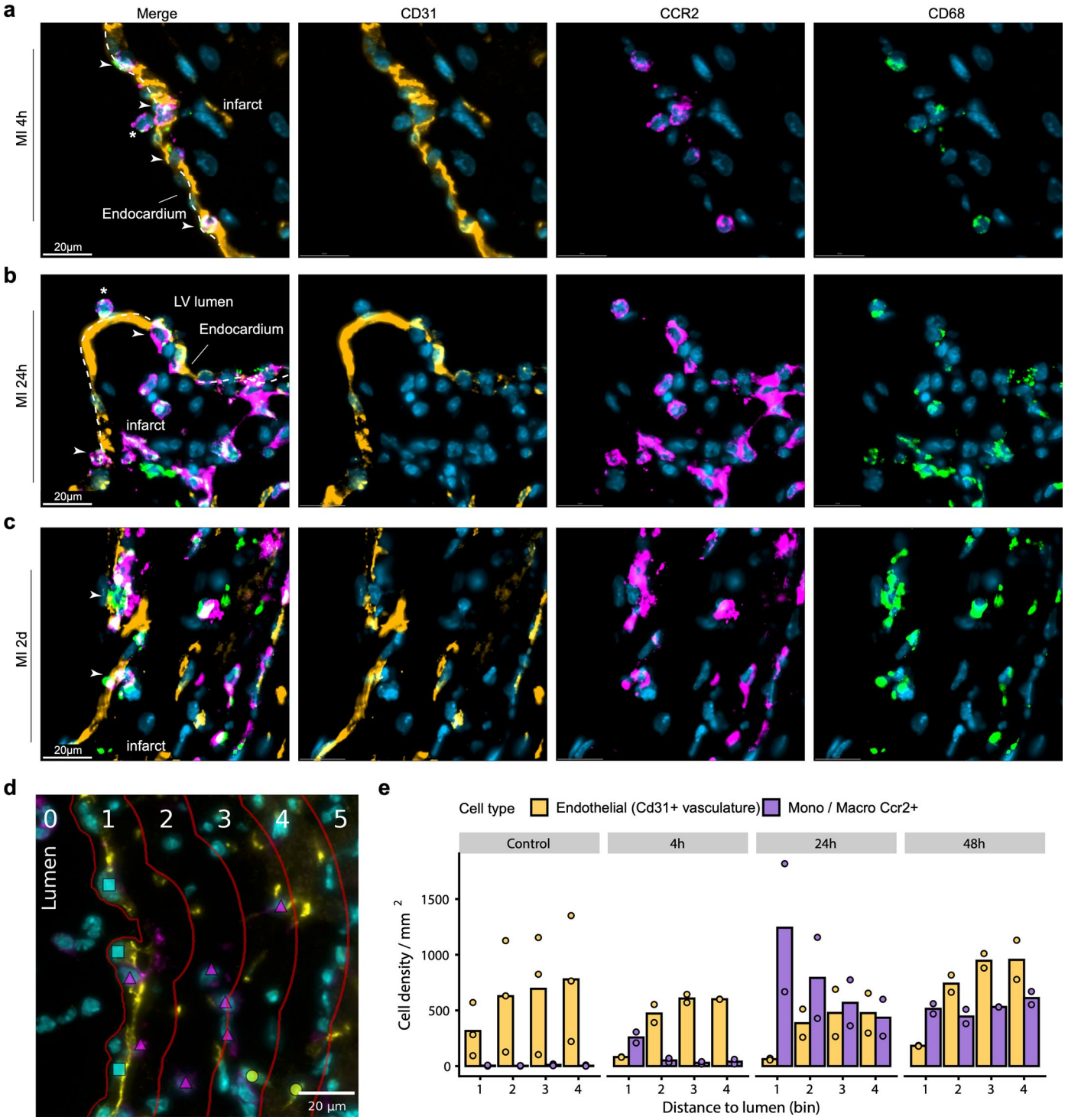

Extended Data Fig. 6 | SeqIF staining of infiltrating Mo/Mϕ in the endocardial layer after MI and quantification of Mo/Mϕ and CD31+ cells of the vasculature from SeqIF data using a binning strategy. a–**c**) Representative SeqIF images showing selected markers including CD31 (yellow), CCR2 (magenta), CD68 (green) and DAPI (blue) with attachment (asterisk) and transmigration (arrow) of CCR2 + CD68+ monocytes/macrophages. **d**) The endocardial infarct zone in SeqIF images was split into bins from lumen towards the infarct core to quantify cells across the bins over time. Cyan: DAPI, yellow: Cd31, magenta: Ccr2, cyan square: endocardial cells, yellow circle: other endothelial cells, magenta triangle: Ccr2+ Mo/Mϕ. **e**) Relative cell abundance in mm2 across different endocardial infarct zone bins from SeqIF shows an increase of Ccr2+ Mo/Mϕ at the endocardial layer around 24 h, while abundance Cd31+ cells of the vasculature remains constant over time.

https://doi.org/10.1038/s44161-025-00717-y

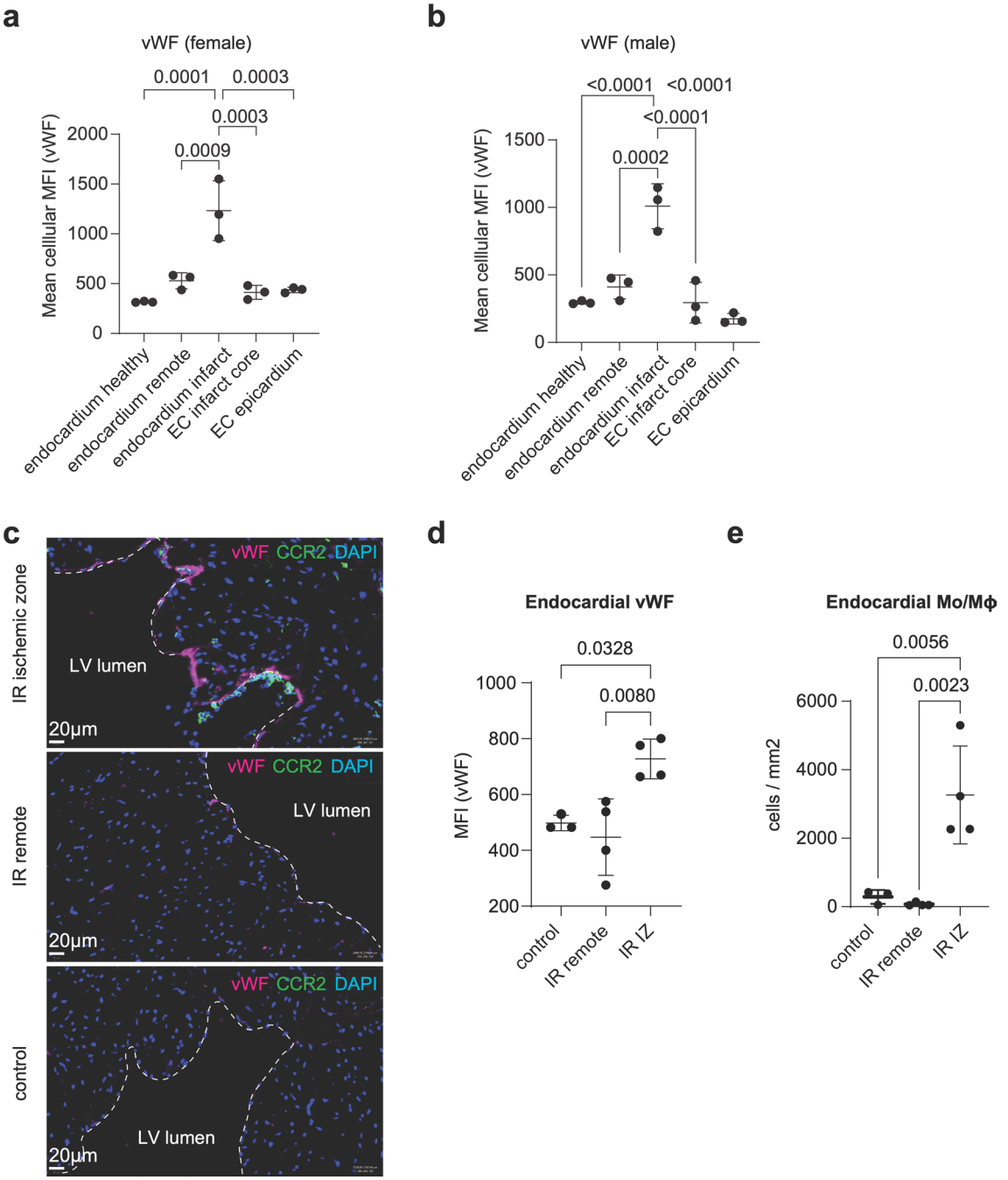

Extended Data Fig. 7 | Immunofluorescent staining of CCR2+ Mo/Mϕ and endocardial vWF after MI and ischemia/reperfusion injury. a, b) Quantification of vWF in different regions 24 h after MI based on immunofluorescence in female and male mice. **c**) Immunofluorescence stainings of CCR2 and vWF in the infarct zone 24 h after ischemia/reperfusion injury. **d**) Quantification of endocardial vWF after ischemia/reperfusion injury. **e**) Quantification of infiltrating Mo/Mϕ at the endocardial region in both control hearts and hearts after ischemia/reperfusion injury.

nature portfolio

Corresponding author(s): Denis Schapiro, Florian Leuschner

Last updated by author(s): Aug 2, 2025

Reporting Summary

Nature Portfolio wishes to improve the reproducibility of the work that we publish. This form provides structure for consistency and transparency in reporting. For further information on Nature Portfolio policies, see our Editorial Policies and the Editorial Policy Checklist.

Statistics

For all statistical analyses, confirm that the following items are present in the figure legend, table legend, main text, or Methods section.

n/a	Confirmed	
☐	☒	The exact sample size (*n*) for each experimental group/condition, given as a discrete number and unit of measurement
☐	☒	A statement on whether measurements were taken from distinct samples or whether the same sample was measured repeatedly
☐	☒	The statistical test(s) used AND whether they are one- or two-sided *Only common tests should be described solely by name; describe more complex techniques in the Methods section.*
☒	☐	A description of all covariates tested
☐	☒	A description of any assumptions or corrections, such as tests of normality and adjustment for multiple comparisons
☐	☒	A full description of the statistical parameters including central tendency (e.g. means) or other basic estimates (e.g. regression coefficient) AND variation (e.g. standard deviation) or associated estimates of uncertainty (e.g. confidence intervals)
☐	☒	For null hypothesis testing, the test statistic (e.g. *F*, *t*, *r*) with confidence intervals, effect sizes, degrees of freedom and *P* value noted *Give P values as exact values whenever suitable.*
☒	☐	For Bayesian analysis, information on the choice of priors and Markov chain Monte Carlo settings
☒	☐	For hierarchical and complex designs, identification of the appropriate level for tests and full reporting of outcomes
☒	☐	Estimates of effect sizes (e.g. Cohen's *d*, Pearson's *r*), indicating how they were calculated

Our web collection on statistics for biologists contains articles on many of the points above.

Software and code

Policy information about availability of computer code

Data collection	Zeiss Zen Blue version 3.2, VisualSonics 3100 Echocardiography System
Data analysis	Vevo LAB 5.7.1, QuPath 0.5.1, GraphPad Prism 10.0, FlowJo 10.9.0. All code used to analyse the data in this manuscript is available publicly at https://github.com/SchapiroLabor/mi_spatialomics.

For manuscripts utilizing custom algorithms or software that are central to the research but not yet described in published literature, software must be made available to editors and reviewers. We strongly encourage code deposition in a community repository (e.g. GitHub). See the Nature Portfolio guidelines for submitting code & software for further information.

Data

Policy information about availability of data

All manuscripts must include a data availability statement. This statement should provide the following information, where applicable:

- Accession codes, unique identifiers, or web links for publicly available datasets
- A description of any restrictions on data availability
- For clinical datasets or third party data, please ensure that the statement adheres to our policy

A data availability statement is included in the manuscript. All relevant images and data for Molecular Cartography and SeqIF described in this study are publicly available via Synapse (project SynID : syn51449054): https://www.synapse.org/#!Synapse:syn54235747. The mass spectrometry proteomics data have been deposited to the ProteomeXchange Consortium via the PRIDE partner repository with the dataset identifier PXD066993.

Research involving human participants, their data, or biological material

Policy information about studies with human participants or human data. See also policy information about sex, gender (identity/presentation), and sexual orientation and race, ethnicity and racism.

Reporting on sex and gender	*Use the terms sex (biological attribute) and gender (shaped by social and cultural circumstances) carefully in order to avoid confusing both terms. Indicate if findings apply to only one sex or gender; describe whether sex and gender were considered in study design; whether sex and/or gender was determined based on self-reporting or assigned and methods used.* *Provide in the source data disaggregated sex and gender data, where this information has been collected, and if consent has been obtained for sharing of individual-level data; provide overall numbers in this Reporting Summary. Please state if this information has not been collected.* *Report sex- and gender-based analyses where performed, justify reasons for lack of sex- and gender-based analysis.*
Reporting on race, ethnicity, or other socially relevant groupings	*Please specify the socially constructed or socially relevant categorization variable(s) used in your manuscript and explain why they were used. Please note that such variables should not be used as proxies for other socially constructed/relevant variables (for example, race or ethnicity should not be used as a proxy for socioeconomic status).* *Provide clear definitions of the relevant terms used, how they were provided (by the participants/respondents, the researchers, or third parties), and the method(s) used to classify people into the different categories (e.g. self-report, census or administrative data, social media data, etc.)* *Please provide details about how you controlled for confounding variables in your analyses.*
Population characteristics	*Describe the covariate-relevant population characteristics of the human research participants (e.g. age, genotypic information, past and current diagnosis and treatment categories). If you filled out the behavioural & social sciences study design questions and have nothing to add here, write "See above."*
Recruitment	*Describe how participants were recruited. Outline any potential self-selection bias or other biases that may be present and how these are likely to impact results.*
Ethics oversight	*Identify the organization(s) that approved the study protocol.*

Note that full information on the approval of the study protocol must also be provided in the manuscript.

Field-specific reporting

Please select the one below that is the best fit for your research. If you are not sure, read the appropriate sections before making your selection.

☒ Life sciences ☐ Behavioural & social sciences ☐ Ecological, evolutionary & environmental sciences

For a reference copy of the document with all sections, see nature.com/documents/nr-reporting-summary-flat.pdf

Life sciences study design

All studies must disclose on these points even when the disclosure is negative.

Sample size	Molecular Cartography was performed using two biological replicates per time point (i.e., two mouse hearts per time point). In addition, a second slide with consecutive sections from the same mouse hearts was analyzed to replace samples from the first slide that did not pass quality control (see Supplementary Figure 1a and Supplementary Figure 2 for a comparison of the two slides). For the final analysis presented in Figures 1 and 2, only the two biological replicates per time point from these two slides were used. For SeqIF (COMET) experiments, 3 biological replicates were used for controls and 2 biological replicates for 4 hours, 24 hours and 2 days. All of the SeqIF samples as well as the conventional immunofluorescence samples are from different mice than the Molecular Cartography experiments and are therefore completely independent. For in-vivo outcome studies, sample size calculations were performed in G*Power 3.1 in accordance with the approved animal protocol and were based on our experience with comparable experimental studies to achieve 80% power at a significance level of 0.05.
Data exclusions	No exclusion of specific animals from the experiments was performed.
Replication	Since findings were consistent across all technologies, experiments were not repeated due to ethical reasons.
Randomization	Mice were randomly assigned to different experimental groups.
Blinding	Echocardiographic and histological analyses were performed in a blinded fashion if applicable.

Reporting for specific materials, systems and methods

We require information from authors about some types of materials, experimental systems and methods used in many studies. Here, indicate whether each material, system or method listed is relevant to your study. If you are not sure if a list item applies to your research, read the appropriate section before selecting a response.

Materials & experimental systems

n/a	Involved in the study
☐	☒ Antibodies
☒	☐ Eukaryotic cell lines
☒	☐ Palaeontology and archaeology
☐	☒ Animals and other organisms
☒	☐ Clinical data
☒	☐ Dual use research of concern
☒	☐ Plants

Methods

n/a	Involved in the study
☒	☐ ChIP-seq
☐	☒ Flow cytometry
☒	☐ MRI-based neuroimaging

Antibodies

Antibodies used

All antibodies used in this studies are listed in supplementary tables 2-4: Trem2 (Abcam ab245227), CD68 (Abcam ab53444), aSMA (Cell Signaling 19245), CD11b (Thermo Fisher 14-0112-82), CD31 (Abcam ab182981), CD45 (Novus Biosciences NB100-77417), Ccr2 (Abcam ab273050), Postn (Abcam ab215199), Pdgfra (Abcam ab203491), Icam1 (Thermo Fisher MA5-43363), LaminB1 (Abcam ab133741), Mpo (Abcam ab208670), Gpnmb (Abcam ab188222), Ankrd1 (Thermo Fisher BS-8074R), Tnnt2 (Thermo Fisher ab209813), WGA-AF555 (Thermo Fisher W32464), anti-CD45-PerCP-Cy5.5 (BD Biosciences clone 30-F11), anti-Ter119-PE (BD Biosciences clone TER-119), anti-CD4-PE (Biolegend clone RM4-5), anti-CD19-PE (BD Biosciences clone 1D3), anti-NK1.1-PE (BD Biosciences clone PK136), anti-Ly6G-PE (BD Biosciences clone 1A8), anti-CD11b-APC-Cy7 (BD Biosciences clone M1/70), anti-F4/80-PE-Cy7 (Biolegend clone BM8), anti-Ly6C-APC (BD Biosciences clone AL-2), vWF (Dako A0082), CD41 (Abcam ab33661), PSGL-1 (BioXCell/Biozol BE0186), CCR2 (Abcam ab273050), CD68 (Abcam ab245227), CD31 (R&D Systems AF3628), anti-Rabbit IgG,Alexa Fluor 555 (Thermo Fisher Scientific A-31572), anti-Goat IgG, Alexa Fluor 555 (Thermo Fisher Scientific A-21432), anti-Rat IgG, Alexa Fluor 647 (Thermo Fisher Scientific A-48272), anti-Rabbit, Alexa Fluor 750 (Abcam ab175728), anti-Rabbit IgG, Alexa Fluor 647 (Thermo Fisher Scientific A-32733), anti-Rabbit IgG, Alexa Fluor 555 (Thermo Fisher Scientific A-32732), anti-Rat IgG, Alexa Fluor 647 (Thermo Fisher Scientific A-48265), anti-Rat IgG, Alexa Fluor 555 (Thermo Fisher Scientific A-48263).

Validation

Antibodies used in this study were from well-established commercial vendors that perform rigorous species-specific QC testing for each lot. Please see details on manufacturers websites (Abcam, Agilent, BD Biosciences, BioXCell, Novus Biosciences, Thermo Fisher Scientific). anti-human vWF antibody A0082 is a validated antibody with reported mouse cross-reactivity (cited in over 1060 publications). For validation of antibodies for SeqIF, performed test stainings at the vendor-recommended concentrations. If staining was too strong or weak, dilution curves were performed, and staining specificity was manually evaluated. The final evaluation was subjective, relying on whether the staining pattern aligned with expectations based on literature and established markers. For challenging markers like Trem2, which tended to form aggregates, larger aggregates were excluded, and coexpression with CD68 was used to confirm specificity. SeqIF requires additional considerations compared to standard immunofluorescence, such as determining the optimal fluorescence channel (e.g., Cy5 or TRITC) and cycle placement. Fluorescence signal acquisition in the Cy5 channel demonstrated higher signal-to-noise ratios and overall cleaner results, whereas the TRITC channel exhibited increased autofluorescence. Of the 16 antibodies tested, 12 were imaged in the Cy5 channel due to the predominance of functional antibodies raised in rabbit (Supplementary Table 2). The panel was finalized after 58 optimization runs, supported by the Lunaphore COMET PA platform for evaluating intensity, sensitivity, elution efficacy, incubation time, antibody dilution, exposure time, and cycle position.

Animals and other research organisms

Policy information about studies involving animals; ARRIVE guidelines recommended for reporting animal research, and Sex and Gender in Research

Laboratory animals

C57BL/6NRj female mice were obtained from Janvier labs (Saint-Berthevin, France) and were studied at 10 - 12 weeks of age. Mice were housed under standard laboratory conditions with a 12h light-dark cycle and access to water and food ad libitum.

Wild animals

No wild animals were used in this study.

Reporting on sex

All experiments in this study were performed in female mice, which is common practice for murine MI models due to higher resilience to cardiac stress. Validation experiments were performed in male mice which confirmed a similar pattern of vWF expression and endocardial monocyte accumulation.

Field-collected samples

No field-collected samples were used in this study.

Ethics oversight

All animal procedures were approved by the institutional review board of the University of Heidelberg, Germany, and the responsible government authority of Baden-Württemberg, Germany (project number G-106/19 and G-94/21).

Note that full information on the approval of the study protocol must also be provided in the manuscript.

Plants

Seed stocks

Report on the source of all seed stocks or other plant material used. If applicable, state the seed stock centre and catalogue number. If plant specimens were collected from the field, describe the collection location, date and sampling procedures.

Novel plant genotypes

Describe the methods by which all novel plant genotypes were produced. This includes those generated by transgenic approaches, gene editing, chemical/radiation-based mutagenesis and hybridization. For transgenic lines, describe the transformation method, the number of independent lines analyzed and the generation upon which experiments were performed. For gene-edited lines, describe the editor used, the endogenous sequence targeted for editing, the targeting guide RNA sequence (if applicable) and how the editor was applied.

Authentication

Describe any authentication procedures for each seed stock used or novel genotype generated. Describe any experiments used to assess the effect of a mutation and, where applicable, how potential secondary effects (e.g. second site T-DNA insertions, mosiacism, off-target gene editing) were examined.

Flow Cytometry

Plots

Confirm that:

☒ The axis labels state the marker and fluorochrome used (e.g. CD4-FITC).

☒ The axis scales are clearly visible. Include numbers along axes only for bottom left plot of group (a 'group' is an analysis of identical markers).

☐ All plots are contour plots with outliers or pseudocolor plots.

☐ A numerical value for number of cells or percentage (with statistics) is provided.

Methodology

Sample preparation

Single-cell suspensions of infarcted hearts were obtained by mincing the tissue with fine scissors and digesting it with a solution containing 450 U/mL collagenase I, 125 U/mL collagenase XI, 60 U/mL DNase I, and 60 U/mL hyaluronidase (MilliporeSigma) for 1 hour at 37°C while shaking. For flow cytometry of blood samples, erythrocytes were lysed in RBC lysis buffer (Miltenyi Biotec). The fluorescent antibodies are described in Supplementary Table 3.

Instrument

Flow cytometry was performed on a FACSVerse (BD Biosciences).

Software

Data was analyzed using FlowJo v10.9.0 software

Cell population abundance

No sorting of certain cell populations was performed.

Gating strategy

Mo/Mϕ were identified as CD45+, Lin-(CD19;CD4;NK1.1;Ly6G;Ter119), CD11b+. Neutrophils were identified as CD45+, Lin+(CD19;CD4;NK1.1;Ly6G;Ter119), CD11b+. Lymphoid cells were gated CD45+, Lin-(CD19;CD4;NK1.1;Ly6G;Ter119), CD11b-.

☒ Tick this box to confirm that a figure exemplifying the gating strategy is provided in the Supplementary Information.